

CaFA: Global Weather ForeCasting with FActorized Attention on Sphere

Zijie Li[†], Anthony Zhou[†], Saurabh Patil[†], Amir Barati Farimani^{†*}
[†] *Mechanical Engineering Department, Carnegie Mellon University*

May 14, 2024

Abstract

Accurate weather forecasting is crucial in various sectors, impacting decision-making processes and societal events. Data-driven approaches based on machine learning models have recently emerged as a promising alternative to numerical weather prediction models given their potential to capture physics of different scales from historical data and the significantly lower computational cost during the prediction stage. Renowned for its state-of-the-art performance across diverse domains, the Transformer model has also gained popularity in machine learning weather prediction. Yet applying Transformer architectures to weather forecasting, particularly on a global scale is computationally challenging due to the quadratic complexity of attention and the quadratic increase in spatial points as resolution increases. In this work, we propose a factorized-attention-based model tailored for spherical geometries to mitigate this issue. More specifically, it utilizes multi-dimensional factorized kernels that convolve over different axes where the computational complexity of the kernel is only quadratic to the axial resolution instead of overall resolution. The deterministic forecasting accuracy of the proposed model on 1.5° and 0-7 days' lead time is on par with state-of-the-art purely data-driven machine learning weather prediction models. We also showcase the proposed model holds great potential to push forward the Pareto front of accuracy-efficiency for Transformer weather models, where it can achieve better accuracy with less computational cost compared to Transformer based models with standard attention.

1 Introduction

Weather forecasting plays a pivotal role in numerous aspects of modern society, spanning from agriculture and transportation to disaster preparedness and public safety. The ability to predict weather conditions accurately allows informed decision making in a wide array of engineering and social events. Numerical weather prediction (NWP) (Bauer et al., 2015), a cornerstone of modern meteorology, utilizes numerical models to simulate the Earth's atmosphere and predict the future weather. The simulation process consists of constructing partial differential equations to describe the global weather dynamics and then solving the equation via numerical algorithms. Resolving finer physical scales, such as simulating microphysics phenomena or using a finer spatio-temporal discretization, allows greater NWP accuracy; however, this greatly increases the computational cost. Performing a 10-day forecast can take an hour on a supercomputer (Bauer et al., 2020; Benjamin et al., 2018). Additionally, accurately resolving small scale physics requires a well-tailored parametrization of the numerical model that approximates the underlying physical process.

The recent progress in machine learning and increasing amount of available data have facilitated the emergence of machine-learning-based weather prediction (MLWP) models. Compared to NWP, MLWP offers the potential to capture and learn finer-scale physics from data without describing the physics in an analytical mathematical model or searching for precise parameterization fits. By ingesting datasets encompassing large amounts of historical weather records, these models can learn and fit intricate patterns and correlations in the global weather dynamics. Recently, MLWP models, particularly those based on deep neural networks, have shown promising potential in global weather prediction (Bi et al., 2023; Lam et al., 2023; Kurth et al.,

*Correspondence: barati@cmu.edu

2023; Chen et al., 2023c,a; Nguyen et al., 2023a,b; Verma et al., 2024; Bonev et al., 2023; Keisler, 2022). They have demonstrated competitive accuracy compared to physics-based numerical models in medium-range weather forecasting. Once trained, they can conduct prediction tasks very efficiently on computing devices (e.g. graphic processing units) specialized for neural network computation. For instance, a 10-day forecast at a scale of around 30 km can be completed within a minute (Bi et al., 2023; Lam et al., 2023; Kurth et al., 2023).

Among different types of neural network architectures, Transformer models based on the attention mechanism (Vaswani et al., 2017) stands out as a notable class. Initially designed for processing sequences in natural language, Transformer models have found successful applications in a wide array of engineering and scientific domains, such as image classification (Dosovitskiy et al., 2021) and protein folding (Jumper et al., 2021). At its essence, the Transformer’s attention mechanism provides the ability to capture non-local patterns at all length scales within the context and employs data-controlled weights to aggregate different features dynamically, with its computational cost scaling quadratically with respect to the context size; this can range from one to the full length of the input data. Prior efforts to reduce the computational cost include linearizing the computational complexity via kernel approximation (Choromanski et al., 2020), hardware-aware optimization of the algorithm implementation (Dao et al., 2022), or sparsifying the attention computation by restricting the context size through partitioning the input into different windows (Beltagy et al., 2020; Liu et al., 2021). For global weather forecasting tasks, previous Transformer-based models apply attention to the input mostly with the spatial structure flattened (Nguyen et al., 2023a,b). Sliding window attention can be used afterwards to restrict the attention context (Chen et al., 2023c; Bi et al., 2023; Chen et al., 2023a) and therefore reduce the computational cost. In these cases, the multi-dimensional (longitude-latitude) spatial structure of the input is not taken into account explicitly. While attending between every pair of tokens that represent embedded features at different locations can exploit all possible interactions in the data, its computation is prohibitively expensive. Another drawback of discarding spatial structure is that useful inductive biases about the underlying physics such as boundary condition and geometry information (the target domain is on a sphere) can not be easily applied, although some of this information can be implicitly encoded to the model, e.g. via positional encoding.

In this work, we explore a different perspective of designing the attention layer, where the multi-dimensional structure is preserved during the attention calculation. We build our model with the low-rank attention kernel operator (Li et al., 2024) that decomposes the multi-dimensional attention kernel into a set of single-dimensional sub-kernels. The sub-kernels are parameterized using dot-product attention with angular distance modulation which facilitates a smooth response of the attention score under varying distances. We numerically validate the deterministic forecasting capability of the proposed model on WeatherBench2 (Rasp et al., 2023)’s data which has a resolution of 1.5° . The proposed model - CaFA (ForeCast with Factorized Attention) outperforms the deterministic operational Integrated Forecast System (IFS) on most investigated variables and shows competitive performance over other state-of-the-art end-to-end MLWPs in 0-7 days’ global weather forecasting. Our study represents a stride towards reducing the computational cost of Transformer-based weather models without sacrificing accuracy, thereby enhancing their accessibility and efficiency.

2 Related Works

The advances in computing and general numerical methods for partial differential equations have revolutionized numerical weather prediction over the last century. The core of numerical modeling of weather lies in describing the complex Earth dynamics including land, sea and atmosphere, as coupled equation systems, or earth system models (ESM) (Hurrell et al., 2013). These equation systems are often simulated via general circulation models (GCM) (Phillips, 1956; Lynch, 2008; Satoh, 2013) numerically. Under-resolved physics in GCMs (sub-grid physics that are beyond the scale of finest discretization) are usually approximated with empirical parameterization schemes (Stensrud, 2007) and adjusted with domain expertise (Sherwood et al., 2014; Webb et al., 2013). Not only have the numerical methods of climate/weather prediction been greatly advanced, the amount of high-quality observed and analyzed data has also increased vastly over the last century. One of the most notable instances is historical data from the European Center for Medium-Range Weather Forecasts (ECMWF) reanalysis v5 (ERA5) (Hersbach et al., 2020), which combines historical observations with results from high-fidelity integrated Forecasting System (IFS) (Wedi et al., 2015). These datasets offer

an alternative for advancements in climate and weather modeling, that is using data-driven models instead of manually adjusting parameterizations to better capture underlying physics. Various machine learning models have been employed to enhance the predictive capabilities of complex atmospheric processes, including earlier models that target specific variables/regions (Gagne et al., 2014; Lagerquist et al., 2017) or global weather variables at relatively coarser resolutions (Dueben and Bauer, 2018; Scher, 2018; Scher and Messori, 2019; Weyn et al., 2019; Rasp and Thuerey, 2021; Weyn et al., 2020). More recently, Keisler (2022) proposes a graph-neural-network-based model for forecasting multiple surface and upper-air variables on 1° resolution with accuracy surpassing many prior MLWPs, which underscores the vast potential of MLWP in enhancing weather prediction accuracy and efficiency. FourCastNet (Kurth et al., 2023) demonstrates the promising forecasting capability and superior inference efficiency of MLWP on 0.25° resolution. Pangu-Weather (Bi et al., 2023) and then GraphCast (Lam et al., 2023) further elevate the accuracy of MLWP to the level such that their medium-range forecast (within 10 days) surpasses the state-of-the-art deterministic NWP on many weather variables. They marked the first milestone where MLWP can outperform NWP in terms of both deterministic forecasting accuracy and inference efficiency at such a high resolution.

Each of these advancements are built upon a specific neural network architecture. FourCastNet, which is built upon Adaptive Fourier Neural Operator (Guibas et al., 2022; Li et al., 2021), employs spectral convolution in the Fourier space to capture interactions in the spatial domain. Followup work with the Spherical Fourier Neural Operator (Bonev et al., 2023) improves and extends this framework by doing the convolution in spherical harmonic space to better account for the underlying spherical geometry. GraphCast scales up the graph neural network in Keisler (2022) and leverages multi-scale message passing to better capture both local and non-local interaction between different spatial points. Pangu-Weather is based on the Swin-Transformer (Liu et al., 2021) that leverages sliding window attention to capture spatial interactions. FuXi (Chen et al., 2023c) and Fengwu (Chen et al., 2023a), which are also based on the Swin Transformer, improves the model’s long-term forecasting accuracy with an improved training strategy and model architectures. In parallel, ClimaX (Nguyen et al., 2023a) proposes a versatile climate modelling framework with a modified Vision Transformer (ViT) (Dosovitskiy et al., 2021) backbone and showcases its ability to address various climate and weather tasks including global weather prediction. Stormer (Nguyen et al., 2023b) scales up ClimaX’s Transformer architecture and proposes to pretrain the model with dynamic lead times to further enhance the long-term forecasting accuracy.

Beyond deterministic regression, the integration of deep-learning-based generative models into weather modeling has also gained traction, including ensemble prediction (Price et al., 2023; Li et al., 2023a), probabilistic forecasting and nowcast (Leinonen et al., 2023; Sønderby et al., 2020; Nath et al., 2023) and down-scaling (Leinonen et al., 2021; Mardani et al., 2023; Chen et al., 2023b). Moreover, machine learning models can also be combined with physics priors to create a hybrid model, which can potentially further improve the robustness and accuracy. A canonical paradigm is using machine learning model to predict the under-resolved processes (Rasp et al., 2018) such as various subgrid physics while using a numerical solver built upon governing equation to solve the overall dynamics propagation. NeuralGCM (Kochkov et al., 2023) presents a pioneering realization of this paradigm with performance on par with state-of-the-art MLWP and NWP in terms of both deterministic and ensemble forecast. Additionally, physics can be incorporated by formulating the system propagation as a specific ordinary differential equation (Verma et al., 2024) to guarantee certain physics constraints like momentum conservation.

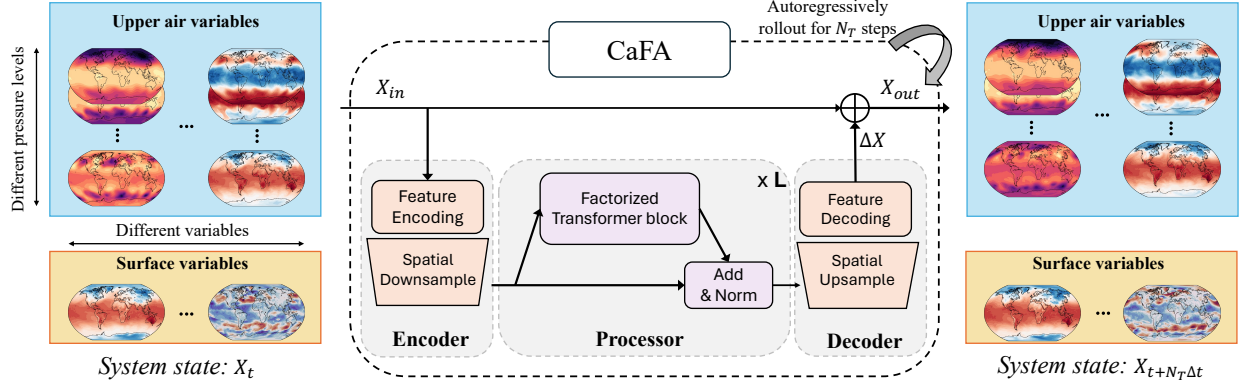


Figure 2.1: Main schematic of the proposed Transformer-based weather forecast model - CaFA. The model approximates a Markovian mapping that forwards the last system state to the next system state with a fixed time interval Δt .

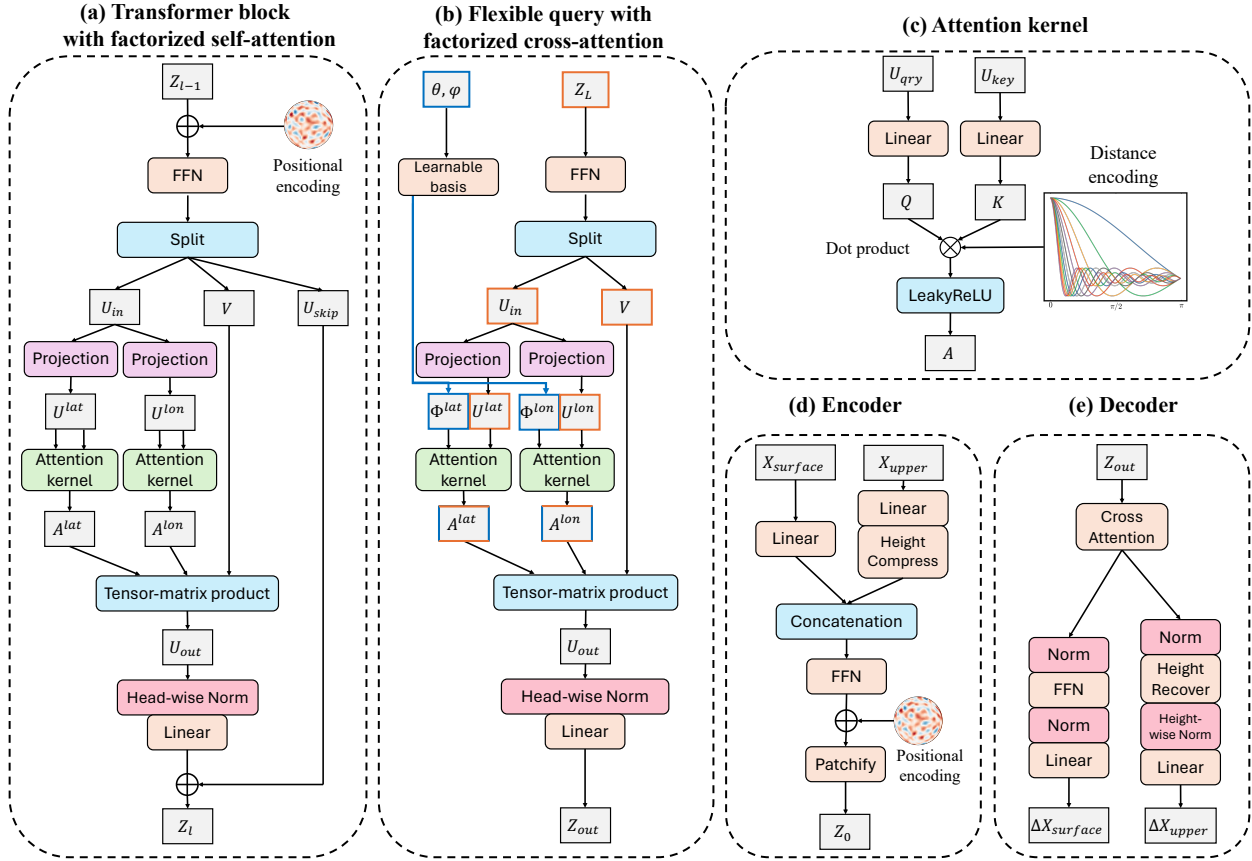


Figure 2.2: Main architecture of the model. **(a)** Each Transformer block in the Processor comprises of a feed-forward network (abbreviated as "FFN", which is a two-layer MLP) and a factorized attention layer. The factorized attention layer contains three major components: projection, attention and tensor-matrix product. **(b)** Cross-attention is used to project the latent embedding on a coarse grid to the high-resolution grid (i.e. upsample). The query location (at longitude θ and latitude φ) can be arbitrary points in the domain. **(c)** Dot-product attention with relative distance encoding. **(d)** The Encoder encodes the input surface variables and upper-air variables into latent embeddings and projects them to a coarser latent grid via patchifying. **(e)** The Decoder projects the latent grid back to the original grid and decodes the latent embedding into surface and upper-air variables' residual.

3 Methodology

3.1 Attention mechanism

The attention mechanism (Bahdanau et al., 2015; Vaswani et al., 2017) has become the core component of modern neural network architectures, revolutionizing various fields including natural language processing (Devlin et al., 2019; Brown et al., 2020) and computer vision (Dosovitskiy et al., 2021). Attention operates on three sets of vectors: queries $\{\mathbf{q}_i\}_{i=1}^{N_q}$, keys $\{\mathbf{k}_i\}_{i=1}^{N_k}$, and values $\{\mathbf{v}_i\}_{i=1}^{N_v}$ ($N_k = N_v$) and computes the weighted average of values:

$$\mathbf{z}_i = \sum_{j=1}^{N_v} h(\mathbf{q}_i, \mathbf{k}_j) \mathbf{v}_j, \quad (1)$$

where $\mathbf{q}_i, \mathbf{k}_i, \mathbf{v}_i \in \mathbb{R}^d$, $h: \mathbb{R}^d \times \mathbb{R}^d \mapsto \mathbb{R}$ is a suitable weight function such as softmax with a scaling factor (Vaswani et al., 2017): $h(\mathbf{q}_i, \mathbf{k}_j) = \exp(\mathbf{q}_i \cdot \mathbf{k}_j / \tau) / \sum_s \exp(\mathbf{q}_i \cdot \mathbf{k}_s / \tau)$ with scaling $\tau = \sqrt{d}$. For self-attention, the query/key/value is transformed from the same input \mathbf{u}_i through a learnable linear transform:

$$\mathbf{q}_i = \mathbf{u}_i W_q, \mathbf{k}_i = \mathbf{u}_i W_k, \mathbf{v}_i = \mathbf{u}_i W_v, \quad (2)$$

where $\mathbf{u}_i \in \mathbb{R}^{d_{in}}$ is the input vector and $W_q, W_k, W_v \in \mathbb{R}^{d_{in} \times d}$ are learnable weight matrices. In cross-attention, queries are usually obtained from a different input source from the keys and values. In its continuous limit, attention in Equation (1) parametrizes a kernel integral transform operator (Kovachki et al., 2023; Cao, 2021). With suitable mesh weights it becomes a Riemann sum approximation of the kernel integral transform:

$$\mathbf{z}_i = \sum_{j=1}^{N_v} h(\mathbf{q}_i \cdot \mathbf{k}_j) \mathbf{v}_j \mu_j \approx \int_{\Omega} \kappa(x_i, \xi) v(\xi) d\xi, \quad (3)$$

where μ_j is the mesh-based weight for grid point x_j , and the weight function h together with dot product of $\mathbf{q}_i, \mathbf{k}_j$ parametrizes the kernel function κ . The application of the attention in modeling a diverse range of PDE-related problems (Cao, 2021; Guo et al., 2023; Li et al., 2023b, 2024; Hao et al., 2023; Liu et al., 2024; Hemmasian and Barati Farimani, 2023; Kissas et al., 2022) suggests its potential for learning the complex global weather dynamics. It is also observed that in Li et al. (2024) the attention matrices of a Transformer trained on PDE problems often have a low-rank structure which motivates us to explore a low-rank parametrization.

3.2 Axial factorized attention on sphere

Factorized attention The original formulation of attention has a complexity $O(N^2)$ (with respect to the total number of grid points N) in terms of its floating point operation. As the number of grid points grows exponentially with respect to the dimension of the problem, the computational cost of applying attention to higher dimensional problems is relatively expensive. To mitigate this issue, Li et al. (2024) proposes an axial-factorized attention leveraging the tensorized structure of data, which comprises two learnable integral operators: axial projection and axial factorized attention. The projection operator projects input functions with a high-dimensional domain Ω into n sub-functions with a single-dimensional domain ($\Omega = \Omega_1 \times \Omega_2 \dots \times \Omega_n$), and then the attention kernels are computed based on projected single-dimensional functions. Below we will introduce their discretized forms.

The projection operator is defined as:

$$\text{Projection: } U_{i^{(m)}}^{(m)} = \gamma \left(\sum_{j^{(1)}=1}^{S_1} \mu_{j^{(1)}}^{(1)} \dots \sum_{j^{(m-1)}=1}^{S_{m-1}} \mu_{j^{(m-1)}}^{(m-1)} \sum_{j^{(m+1)}=1}^{S_{m+1}} \mu_{j^{(m+1)}}^{(m+1)} \dots \sum_{j^{(n)}=1}^{S_n} \mu_{j^{(n)}}^{(n)} U_{j^{(1)}j^{(2)}\dots i^{(m)}\dots j^{(n)}} \right), \quad (4)$$

where $U^{(m)} \in \mathbb{R}^{S_m \times d}$ is the projected feature along the m -th axis, d is the number of feature channels, U is obtained from input tensor $Z \in \mathbb{R}^{S_1 \times \dots \times S_n \times d}$ via a pointwise linear transformation, S_m denotes the size of the grid that discretizes sub-domain Ω_m with $\mu_{j^{(m)}}^{(m)}$ being the corresponding mesh weights for grid point $j^{(m)}$, and $\gamma: \mathbb{R}^d \mapsto \mathbb{R}^d$ is a pointwise two-layer multi-layer perceptron.

Based on the projected functions with a single-dimensional domain, the (self) axial factorized attention

is computed as follows:

$$\text{Axial attention kernel: } A^{(m)} = Q^{(m)}(K^{(m)})^T, \text{ where: } Q^{(m)} = U^{(m)}W_q^{(m)}, K^{(m)} = U^{(m)}W_k^{(m)}, \quad (5)$$

$$\begin{aligned} \text{Tensor-matrix product: } & (Z_{\text{out}})_{i^{(1)}i^{(2)}\dots i^{(n)}} \\ &= \sum_{i^{(1)}=1}^{S_1} \mu_{j^{(1)}}^{(1)} A_{i^{(1)}j^{(1)}}^{(1)} \sum_{i^{(2)}=1}^{S_2} \mu_{j^{(2)}}^{(2)} A_{i^{(2)}j^{(2)}}^{(2)} \dots \sum_{i^{(n)}=1}^{S_n} \mu_{j^{(n)}}^{(n)} A_{i^{(n)}j^{(n)}}^{(n)} V_{j^{(1)}j^{(2)}\dots j^{(n)}}, \end{aligned} \quad (6)$$

where $A^{(m)} \in \mathbb{R}^{S_m \times S_m}$ is the m -th axial kernel computed with dot product attention, V is the value tensor which is derived from the input via a learnable linear transformation following standard attention (Equation (2)), and $W_q^{(m)}, W_k^{(m)}$ are learnable linear transformation matrices for computing queries and keys. In Li et al. (2024), all the problems considered have a uniform equi-spaced grid, thus the mesh weight on each grid point along m -th axis is $\mu_j^{(m)} = 1/S_m, \forall j \in \{1, 2, \dots, S_m\}$ and the weighted sum in Equation (4) simply amounts to average pooling over all but the m -th axis. With an equi-angular grid on the spherical domain \mathbb{S}^2 and assuming uniform quadrature rule, the mesh weight on each latitude grid point is non-uniform. Given a latitude coordinate $\varphi \in [-\pi/2, \pi/2]$ and longitude coordinate $\theta \in [0, 2\pi)$ (and assuming unit radius), the integration of function $f : \mathbb{S}^2 \mapsto \mathbb{R}$ on the sphere takes the form:

$$\int_{\mathbb{S}^2} f dS = \int_0^{2\pi} \int_{-\pi/2}^{\pi/2} f \cos \varphi d\varphi d\theta, \quad (7)$$

where a suitable mesh weight for each latitude grid point (cell) j is $\mu_j^{(\text{lat})} = \frac{\pi}{N_{\text{lat}}} \cos \varphi_j$ and $\mu_j^{(\text{lon})} = \frac{2\pi}{N_{\text{lon}}}$ for a longitude grid point on an equi-angular grid. In summary, the vanilla attention-based kernel integral in Equation (3) has now been modified to:

$$z(\theta_i, \varphi_i) = \int_0^{2\pi} \kappa_{\text{lon}}(\theta_i, \theta) \int_{-\pi/2}^{\pi/2} \kappa_{\text{lat}}(\varphi_i, \varphi) v(\varphi) \cos \varphi d\varphi d\theta, \quad (8)$$

with latitudinal kernel and longitudinal kernel $\kappa_{\text{lon}}, \kappa_{\text{lat}}$ parameterized using dot product attention with angular distance modulation which will be described in the next paragraph. Illustrative figures comparing factorized attention and standard attention are provided in Appendix Figure C.3, C.4, C.5.

Distance encoding and positional encoding The original dot-product attention mechanism does not explicitly take the relative position between different points into account, but it is found that modulating the attention with relative position information between tokens is often beneficial (Su et al., 2024; Li et al., 2023b). In this work we propose to use a learnable distance encoding function to directly modulate the dot product between queries and keys:

$$A_{ij}^{(m)} = \sum_{c=1}^d \psi_c^{(m)}(e_{ij}^{(m)}) Q_{ic}^{(m)} K_{jc}^{(m)} \quad (9)$$

where $Q^{(m)}, K^{(m)} \in \mathbb{R}^{S_m \times d}$ are query and key matrices of m -th axis (Equation (5)), $e_{ij}^{(m)}$ is the absolute angular distance along m -th axis between point i and j , and $\psi_c^{(m)} : \mathbb{R} \mapsto \mathbb{R}$ is a learnable function. To parameterize $\psi_c^{(m)}$, we use a Bessel basis function with learnable coefficients (Gasteiger et al., 2019), which previously have shown to be very effective for modelling atomic interactions (Gasteiger et al., 2019, 2021) (here we omit superscript (m) for better readability):

$$\psi_c(e_{ij}) = b_c + \sum_{n=1}^{N_{\text{basis}}} W_{nc} \sqrt{\frac{2}{\pi}} \frac{\sin(ne_{ij})}{e_{ij}}, \quad (10)$$

where $e_{ij} \in [0, \pi]$ (in practice we add a small number to the left endpoint to avoid overflow), in which the longitude difference $\theta_{ij} = |\theta_i - \theta_j|$ is wrapped into $[0, \pi]$: $e_{ij} = \min(\theta_{ij}, 2\pi - \theta_{ij})$, and W_{nc}, b_c are a learnable scalar coefficient and offset. For all the experiments, we set $N_{\text{basis}} = 64$ along the longitude direction and $N_{\text{basis}} = 32$ along the latitude direction. After relative distance encoding, we propose to apply a element-wise non-linearity function- leakyReLU (leaky rectified linear unit) to the attention matrix in Equation (9), which suppresses the magnitude of the negative part in the matrix and in practice we find this slightly improves the performance. This also coincides with the observation in Choromanski et al. (2020), where they use ReLU to replace Softmax in the attention kernel and observe performance improvement.

In addition to the relative distance encoding, we also apply learnable absolute positional encoding to the

feature embedding before every Transformer block. The learnable positional encoding is computed by first wrapping the longitude/latitude coordinates with real-valued spherical harmonics and then feeding them to a two-layer MLP. The spherical harmonics can be viewed as an extension of the popular Fourier positional encoding (Vaswani et al., 2017) on flat Euclidean space to the spherical domain \mathbb{S}^2 , which generally improves the performance of coordinate-based networks on spheres (Rußwurm et al., 2024; Elhag et al., 2024). Example visualization of learned attention kernels, distance and positional encoding are shown in Appendix C.

3.3 Grid projection

To reduce the computational cost and improve model scalability, the majority of the proposed model (Processor) operates on a latent grid with reduced resolution. For the height dimension (different pressure levels), the Encoder will project 3D variables onto a 2D surface via a height compression module and then in the Decoder the 3D structure of upper-air variables is recovered via a height recovery module. For the spatial dimension (longitudinal and latitudinal), the 2D grid is uniformly downsampled in the Encoder and then re-projected to the original grid via cross-attention in the Decoder.

Height compression/recovery The height compression is achieved via a 1D height-wise convolution filter, with kernel size equaling the number of pressure levels. To recover the height, we first expand the number of channels of the latent embedding by the number of pressure levels via a linear transformation: $d \mapsto N_{\text{levels}}d$, and then reshape the tensor from $N_{\text{lat}} \times N_{\text{lon}} \times (N_{\text{levels}}d)$ to $N_{\text{lat}} \times N_{\text{lon}} \times N_{\text{levels}} \times d$. After recovering the 3D structure, we apply height-wise learnable linear modulation (Perez et al., 2018) to the features: $\hat{Z}_{...lc} = \alpha_{lc}Z_{...lc} + \beta_{lc}$, $l \in \{1, 2, \dots, N_{\text{levels}}\}, c \in \{1, 2, \dots, d\}$, where $\hat{Z}, Z \in \mathbb{R}^{N_{\text{lat}} \times N_{\text{lon}} \times N_{\text{levels}} \times d}$ are 3D latent embeddings, and α_{lc}, β_{lc} are learnable scalar scaling and offset.

Spatial downsample/upsample We use patchification to downsample the spatial resolution, which is a widely adopted technique in the vision Transformer (Dosovitskiy et al., 2021) to downsample the data resolution and is also used in prior weather forecasting Transformer models. The patchification amounts to applying non-overlapping convolution to the input, with kernel size and stride equal to the patch size p (single-sided zero padding is used when the resolution is not divisible by p). This process downsamples the grid resolution from $N_{\text{lat}} \times N_{\text{lon}}$ to $(N_{\text{lat}}/p) \times (N_{\text{lon}}/p)$.

To recover the original resolution, we use factorized cross-attention (Figure 2.2(b)) to project the low-resolution latent grid back to the original resolution, which is different from previous works that first apply linear transformation to the channel dimension and then reshape it to "un-patchify" the features. The proposed cross-attention module learns a continuous representation (Mildenhall et al., 2020) for the target variables and allows querying at arbitrary locations instead of a fixed resolution grid, which can be useful for downstream applications such as data downscaling and regional forecasting. The longitudinal and latitudinal basis functions are parameterized by SIREN (Sitzmann et al., 2020) - a MLP with a sine activation function, which works well in approximating and representing continuous signals, especially their high-frequency components.

3.4 Model overview

Architecture We use an Encoder-Processor-Decoder (EPD) model architecture (Sanchez-Gonzalez et al., 2020; Lam et al., 2023) (Figure 2.1). The model $F_{\theta}(\cdot)$ predicts the change of the variable ΔX over a fixed time interval Δt given X_t , i.e. $\hat{X}_{t+\Delta t} = f(X_t) = X_t + F_{\theta}(X_t)$. Long-term forecasting is generated by an auto-regressive rollout for multiple steps:

$$\hat{X}_{t+N_T\Delta t} = \underbrace{f \circ f \circ \dots \circ f}_{\times N_T}(X_t). \quad (11)$$

The Encoder takes the surface variables and upper-air variables as input and fuses them together. The 3D upper-air variables are first projected onto a 2D surface via the height compression operation and then concatenated with the surface variable embedding. After concatenation, the surface and upper-air variable embeddings are fused together via a two-layer MLP and then downsampled to the reduced-resolution grid via patchification.

The Processor is a stack of Transformer blocks (we use 6 blocks across all the experiments) operating on the latent grid, where each block comprises of a two-layer MLP (also known as feed forward network, FFN)

followed by the factorized attention layer. We place FFN in front of attention layer contrary to many existing Transformer architectures that place FFN after the attention layer. The main reason is that we aim to fuse positional encoding with features via non-linear transformation before doing the attention, which we found performs slightly better. We use residual connections (He et al., 2016) between different Transformer blocks and inside the attention layer (Figure 2.2 (a)). Layer-normalization (Ba et al., 2016) is applied after the residual connection between each Transformer block (which is known as a post-norm scheme in Transformer literatures). We add layer-normalization after projecting features into queries and keys.

The Decoder takes the latent embedding output from the processor (represented on a reduced resolution grid) as input and decodes it into the 2D surface and 3D upper-air variables. The latent embedding is first upsampled via cross-attention, and then passed into two separate MLPs, where the first one is used to decode the embedding to 2D surface variables and the second is used to project and decode the 2D embedding to 3D upper-air variables.

Training We train the model by employing a curriculum that first minimizes the single-step prediction loss and then multi-step prediction loss, similar to prior works (Lam et al., 2023; Chen et al., 2023a,c; Nguyen et al., 2023b; Kurth et al., 2023). In the first stage, we train the model for 160k gradient steps, where in the first 50k steps the loss is computed on a single step of prediction-target pairs $(\hat{X}_{t+\Delta t}, X_{t+\Delta t})$, and for the remaining 110k steps the loss is computed based on a two-step rollout of predictions $([\hat{X}_{t+\Delta t}, \hat{X}_{t+2\Delta t}], [X_{t+\Delta t}, X_{t+2\Delta t}])$. During the second stage, we train the model for 50k gradient steps and increase the model training rollout steps from 4 to 20 with a curriculum. The training loss function is a latitude and variable weighted $L1$ loss. The motivation for choosing $L1$ loss over $L2$ loss is to reduce the blurriness of the model’s prediction. However, it can make long-term predictions to have higher MSE which we mitigate with multi-step loss during training. The latitude weight and variable weight are computed similar to Lam et al. (2023). The training of the final model on the 1.5° resolution grid is carried out with 4 A6000 GPUs using Distributed Data Parallel and float32 precision, which takes roughly a week. It takes around 6 seconds to generate the prediction up to a week (28 steps) on a single A6000 using float32 precision, with model wrapped by `torch.compile`. We provide a brief summary of the model’s major hyperparameters in Table 3.1, and the model has around 200 M trainable parameters in total. Further details about model training are deferred to the Appendix A.1.

The proposed model is developed and validated based on the ERA5 reanalysis data (Hersbach et al., 2020) from the European Centre for Medium-Range Weather Forecasts (ECMWF), where we use the preprocessed version from WeatherBench2 (Rasp et al., 2023). Similar to GraphCast (Lam et al., 2023), during the model development stage we train the model on 1979 – 2015 and validate on 2016. The final model (on the 1.5° grid) is trained on 1979 – 2019 with data from four additional recent years added to the training dataset.

| Hyperparameter | Value |
|---|--------------|
| Base hidden dimension | 256 |
| Processor hidden dimension | 768 |
| Number of Transformer blocks | 6 |
| Self-attention heads | 16 |
| Self-attention head dimension | 128 |
| Cross-attention heads | 32 |
| Cross-attention head dimension | 128 |
| Latent grid downsample ratio (patch size) | 2×2 |

Table 3.1: Major hyperparameter choices of the model. *Base hidden dimension* denotes the width of MLPs and number of channels of the latent embedding in Encoder and Decoder. In the patchification layer, the latent embedding’s channel size is projected to *Processor hidden dimension* and re-projected back in the Decoder’s upsampling (cross-attention) layer. For the FFN inside each Transformer block, the expansion ratio is set to 6, i.e. the hidden units number is 6 times the input channel number. Gaussian Linear Error Units (GELUs) (Hendrycks and Gimpel, 2023) is used as the non-linear activation inside every Transformer block.

4 Experiments and Results

4.1 Evaluation setting

| Constants | Surface variables | Upper-air variables |
|---------------------------------------|---------------------------------|----------------------------|
| Land sea mask | 2m temperature ($t2m$) | Geopotential (zX) |
| Soil type | 10m u of wind ($u10m$) | Temperature (tX) |
| Angle of sub-gridscale orography | 10m v of wind ($v10m$) | u of wind (uX) |
| Anisotropy of sub-gridscale orography | Mean sea level pressure (MSLP) | v of wind (vX) |
| | Total precipitation 6hr (TP6) | Specific humidity (qX) |
| | Total precipitation 24hr (TP24) | |

Table 4.1: Weather variables used by the model. Surface and upper-air variables are time-dependent variables predicted by the model given an initial condition. 13 pressure levels of upper-air variables are considered: 50, 100, 150, 200, 250, 300, 400, 500, 600, 700, 850, 925, 1000 hPa. X denotes the pressure level in the abbreviation of upper-air variables, e.g. $z500$ denotes geopotential at 500hPa.

Variables and their corresponding abbreviations are listed in Table 4.1. The time resolution is $\Delta t = 6\text{hr}$. The major deterministic metrics are root mean squared error (RMSE), anomaly correlated coefficient (ACC), and bias (see Appendix A.2 for definitions). All the metrics are weighted by the corresponding cell area based on latitude (Lam et al., 2023; Rasp et al., 2023):

$$w(i) = \frac{(\sin \varphi_i^u - \sin \varphi_i^l)}{\frac{1}{N_{\text{lat}}} \sum_{j=1}^{N_{\text{lat}}} (\sin \varphi_j^u - \sin \varphi_j^l)}, \quad (12)$$

where φ_u, φ_l are the corresponding upper/lower latitudinal boundaries for each cell. We exclude the evaluation of total precipitation, as prior works (Lam et al., 2023; Lavers et al., 2022) have suggested the bias of ERA5 precipitation data and its skewed distribution makes deterministic metric like RMSE less meaningful. For MLWP, all the metrics are computed by comparing model’s prediction against ERA5 data. For IFS HRES and IFS ENS (ensemble mean), their evaluation metrics are computed by comparing model’s prediction against IFS analysis data following WeatherBench 2.

The major model is trained on a 1.5° resolution equi-angular grid (240×121) and evaluated on the same grid following the deterministic evaluation protocol in WeatherBench 2 (Rasp et al., 2023). The initial time for each prediction rollout is 00:00/12:00 UTC of every day in year 2020. To compare our model to the open-sourced weather-forecast Transformer - ClimaX (Nguyen et al., 2023a), a ViT (Dosovitskiy et al., 2021) based model that is customized for climate related tasks with a competitive accuracy on coarse resolution. We also train our model on a 64×32 (5.625°) grid following the splitting and testing strategy in Nguyen et al. (2023a). Other MLWP baseline models considered are Pangu-Weather (Pangu) (Bi et al., 2023), FuXi (Chen et al., 2023c) and GraphCast (Lam et al., 2023), which represent the state-of-the-art purely data-driven MLWP. All three models are trained on a 0.25 resolution grid with evaluation results projected to a 1.5° grid (Rasp et al., 2023). Pangu trains different lead time models ($1h, 3h, 6h, 24h$) and cascade them during inference to generate a final prediction. FuXi scales up the number of Swin Transformer (Liu et al., 2021) blocks compared to Pangu (48 vs 16). Instead of cascading models with different lead times, FuXi uses a fixed $6h$ lead time but fine-tunes separate models for different time scales and cascade them during prediction. GraphCast is built upon a multi-resolution graph on the spherical geometry and uses a model with lead time $6h$ to autogressively generate predictions.

4.2 Discussion

The quantitative results for different models’ prediction accuracies are presented in Table 4.2 and 4.3. For pressure variables ($z500$, MSLP), we observe that CaFA consistently outperforms other MLWP baseline within the range of 5 days. For other target variables, CaFA falls behind GraphCast and FuXi for 1 day prediction but gradually catches up. We hypothesize the primary reason is that compared to these models, CaFA is

trained on lower resolution data (1.5° vs 0.25°) and therefore does not have access to finer scale physics which can be important for features like the wind velocity field. The influence of finer-scale physics will gradually diminish as time evolves. This is due to the chaotic nature of weather dynamics and deterministic ML models will tend to approximate the statistical mean which usually dampens the high frequency components (Bonavita, 2023). In general, CaFA is on par with other MLWP baselines for prediction from 3 days up to a week and performs particularly well in variables that features a decaying spectrum such as geopotential. It is also a more lightweight Transformer-based model compared to FuXi, which uses 48 Transformer blocks with hidden dimension 1536 (each block comprises an attention layer and a FFN) in total whereas CaFA uses 6 Transformer blocks plus 1 cross-attention layer with hidden dimension 768.

| Variables | z500 [kg^2/m^2] | | | | t850 [K] | | | | t2m [K] | | | | MSLP [Pa] | | | |
|-------------|-----------------------------------|-----|-----|-----|----------|------|------|------|---------|------|------|------|-----------|-----|-----|-----|
| | 24 | 72 | 120 | 168 | 24 | 72 | 120 | 168 | 24 | 72 | 120 | 168 | 24 | 72 | 120 | 168 |
| IFS HRES | 42 | 135 | 304 | 521 | 0.62 | 1.15 | 1.79 | 2.59 | 0.51 | 0.87 | 1.33 | 1.88 | 60 | 149 | 309 | 506 |
| IFS ENS | 42 | 132 | 277 | 439 | 0.63 | 1.09 | 1.59 | 2.14 | 0.56 | 0.86 | 1.20 | 1.58 | 62 | 146 | 280 | 423 |
| CaFA(Ours) | 39 | 123 | 269 | 449 | 0.60 | 0.99 | 1.56 | 2.28 | 0.55 | 0.84 | 1.24 | 1.76 | 48 | 130 | 271 | 438 |
| Pangu | 44 | 133 | 294 | 501 | 0.61 | 1.03 | 1.68 | 2.47 | 0.56 | 0.91 | 1.39 | 1.97 | 55 | 143 | 297 | 486 |
| FuXi | 40 | 125 | 276 | 433 | 0.54 | 0.95 | 1.56 | 2.11 | 0.53 | 0.84 | 1.27 | 1.65 | 49 | 132 | 276 | 416 |
| GraphCast | 39 | 124 | 274 | 468 | 0.51 | 0.93 | 1.53 | 2.29 | 0.51 | 0.82 | 1.25 | 1.81 | 48 | 132 | 276 | 454 |
| Climatology | 820 | 820 | 820 | 820 | 3.41 | 3.41 | 3.41 | 3.41 | 2.61 | 2.61 | 2.61 | 2.61 | 725 | 725 | 725 | 725 |

Table 4.2: Deterministic forecast RMSE on year 2020’s data for temperature and pressure at different lead times. Darker colors indicate better performance. The evaluation results for baseline models are taken from WeatherBench2 (Rasp et al., 2023).

| Variables | q700 [g/kg] | | | | u850 [m/s] | | | | v850 [m/s] | | | | u10m [m/s] | | | | v10m [m/s] | | | |
|-------------|-------------|------|------|------|------------|------|------|------|------------|------|------|------|------------|------|------|------|------------|------|------|------|
| | 24 | 72 | 120 | 168 | 24 | 72 | 120 | 168 | 24 | 72 | 120 | 168 | 24 | 72 | 120 | 168 | 24 | 72 | 120 | 168 |
| IFS HRES | 0.56 | 0.97 | 1.28 | 1.54 | 1.18 | 2.32 | 3.65 | 4.99 | 1.20 | 2.34 | 3.69 | 5.07 | 0.83 | 1.61 | 2.56 | 3.50 | 0.87 | 1.67 | 2.66 | 3.66 |
| IFS ENS | 0.51 | 0.84 | 1.06 | 1.22 | 1.14 | 2.10 | 3.13 | 4.03 | 1.16 | 2.12 | 3.16 | 4.08 | 0.81 | 1.47 | 2.19 | 2.82 | 0.84 | 1.51 | 2.27 | 2.95 |
| CaFA(Ours) | 0.55 | 0.84 | 1.07 | 1.30 | 1.11 | 1.98 | 3.09 | 4.24 | 1.12 | 2.00 | 3.13 | 4.30 | 0.69 | 1.34 | 2.16 | 2.98 | 0.72 | 1.39 | 2.24 | 3.12 |
| Pangu | 0.54 | 0.88 | 1.20 | 1.48 | 1.17 | 2.11 | 3.38 | 4.70 | 1.19 | 2.15 | 3.44 | 4.79 | 0.73 | 1.43 | 2.36 | 3.28 | 0.76 | 1.49 | 2.45 | 3.44 |
| FuXi | - | - | - | - | 1.03 | 1.96 | 3.15 | 3.96 | 1.05 | 2.00 | 3.21 | 4.03 | 0.66 | 1.33 | 2.19 | 2.74 | 0.69 | 1.38 | 2.28 | 2.87 |
| GraphCast | 0.47 | 0.80 | 1.06 | 1.31 | 1.00 | 1.94 | 3.12 | 4.36 | 1.02 | 1.97 | 3.17 | 4.43 | 0.65 | 1.32 | 2.18 | 3.05 | 0.68 | 1.37 | 2.26 | 3.19 |
| Climatology | 1.61 | 1.61 | 1.61 | 1.61 | 5.66 | 5.66 | 5.66 | 5.66 | 5.47 | 5.47 | 5.47 | 5.47 | 3.83 | 3.83 | 3.83 | 3.83 | 3.96 | 3.96 | 3.96 | 3.96 |

Table 4.3: Deterministic forecast RMSE for specific humidity and wind speed components at different lead times and pressure levels on year 2020’s data.

As shown in Figure 4.2 and 4.3, CaFA has lower RMSE and higher ACC than IFS HRES from 1 to 7 days on most of the target variables. Comparing to the ensemble mean of IFS forecasts, CaFA’s performance is on par or better up to 5 days, but after 5 days the ensemble mean generally has better accuracy. We find that for CaFA, using a larger time step size can improve forecasting accuracy beyond 7 days by trading off accuracy within 7 days range (the comparison is shown in Appendix C.2). We also analyze the upper-air variables’ prediction of different pressure levels by comparing it to IFS HRES prediction. Figure 4.1 shows that CaFA has better RMSE across most pressure levels except for 50hPa, where HRES consistently performs better. Such a trend is also observed in GraphCast (Lam et al., 2023) and one of the reason is that both CaFA and GraphCast are trained on loss that outweighs near-surface (higher pressure) accuracy over smaller pressure levels’ accuracy. An example rollout visualization of 3 key variables is shown in Figure 4.4, qualitatively the models’ prediction agrees well with reference ERA5 analysis data in terms of the general pattern. On the wind velocity field, it is observed that the high-frequency details are blurrier as lead time increases. Visualizations of other variables are shown in Appendix C.

We also compare our model to ClimaX (Nguyen et al., 2023a) * to better understand the influence of

*ClimaX’s official code for model and its training is publicly available (with MIT license) at: <https://github.com/microsoft/ClimaX/tree/main>.

different attention mechanisms. To factor out the influence of discretization (in space and time) and feature selection, we slightly modify the original ViT-based architecture in ClimaX to train an autoregressive model (the resulting model is called ClimaX-AR) with lead time equal to 6 hours using the weather variables specified in Table 4.1 (which uses more atmospheric variables than original ClimaX). This ensures an exact same training pipeline between CaFA and ClimaX-AR. We observe ClimaX-AR performs notably better than the direct prediction version used in original ClimaX, particularly at shorter lead times. As shown in Table 4.4, equipped with factorized attention, CaFA performs consistently better on four key variables for lead time 1-7 days, using significantly smaller amount of FLOPs. We also provide a computational benchmark comparing factorized attention and standard attention on different resolution grid in the Appendix B.3, which shows that factorized attention greatly reduces the computational cost associated with higher resolution grid. This highlights that the potential of proposed factorized attention in improving the efficiency/accuracy balance of Transformer-based weather models.

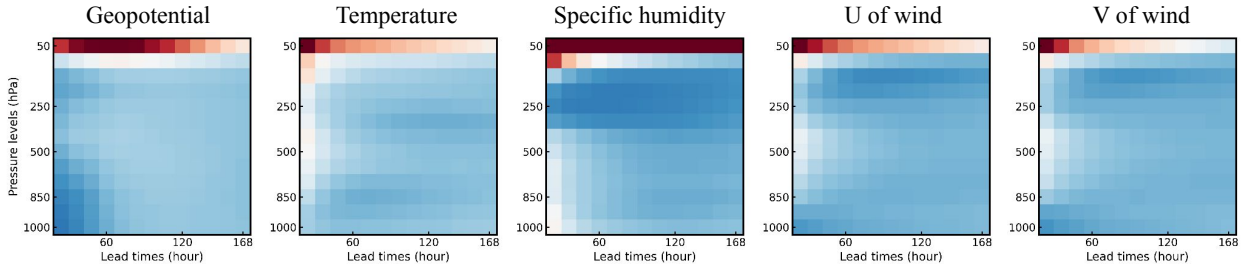


Figure 4.1: Normalized RMSE difference: $(\text{RMSE}_{\text{HRES}} - \text{RMSE}_{\text{CaFA}})/\text{RMSE}_{\text{HRES}}$. Blue colors indicate IFS HRES has larger RMSE while red colors indicate CaFA has larger RMSE. Darker colors indicate a larger normalized difference. The plotting style follows GraphCast (Lam et al., 2023).

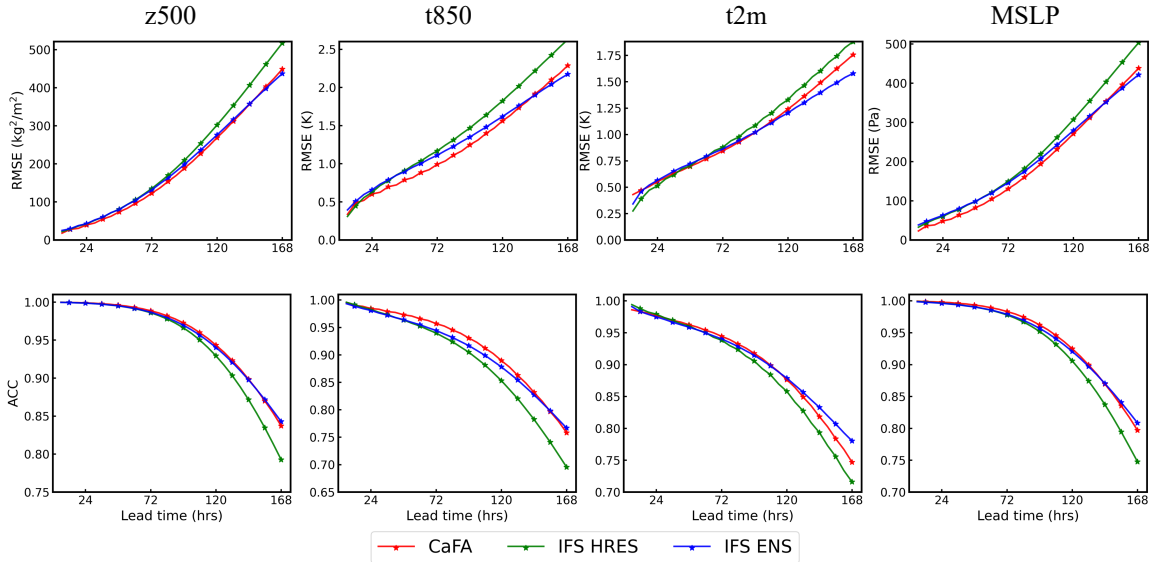


Figure 4.2: Comparison of CaFA and NWP in temperature and pressure’s prediction of year 2020.

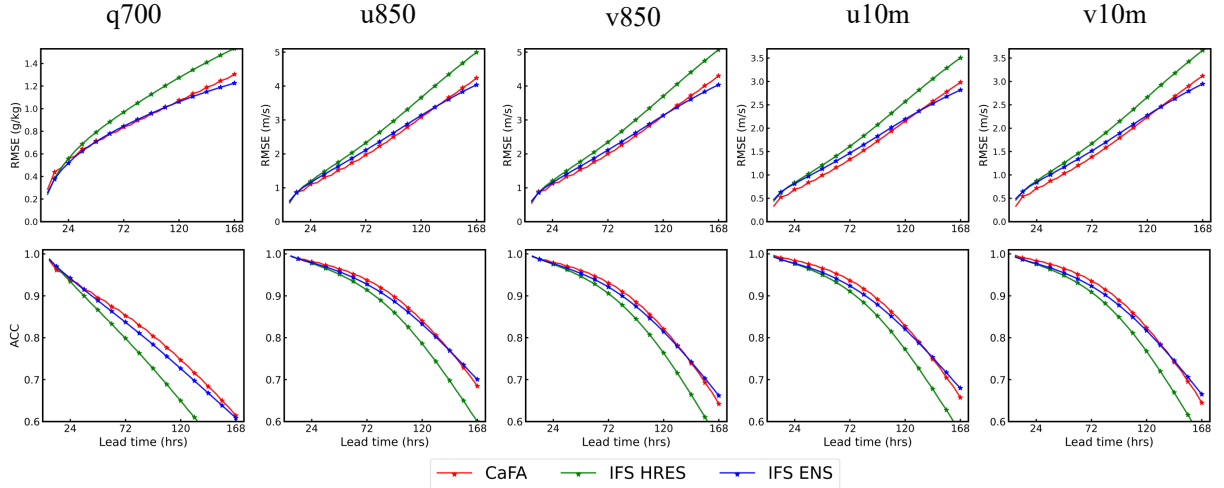
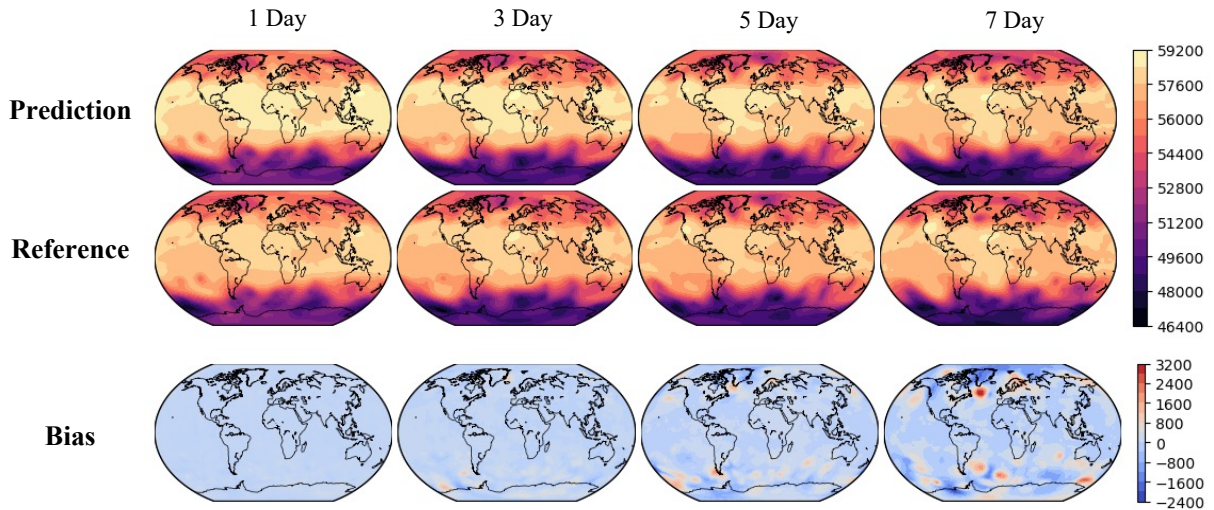


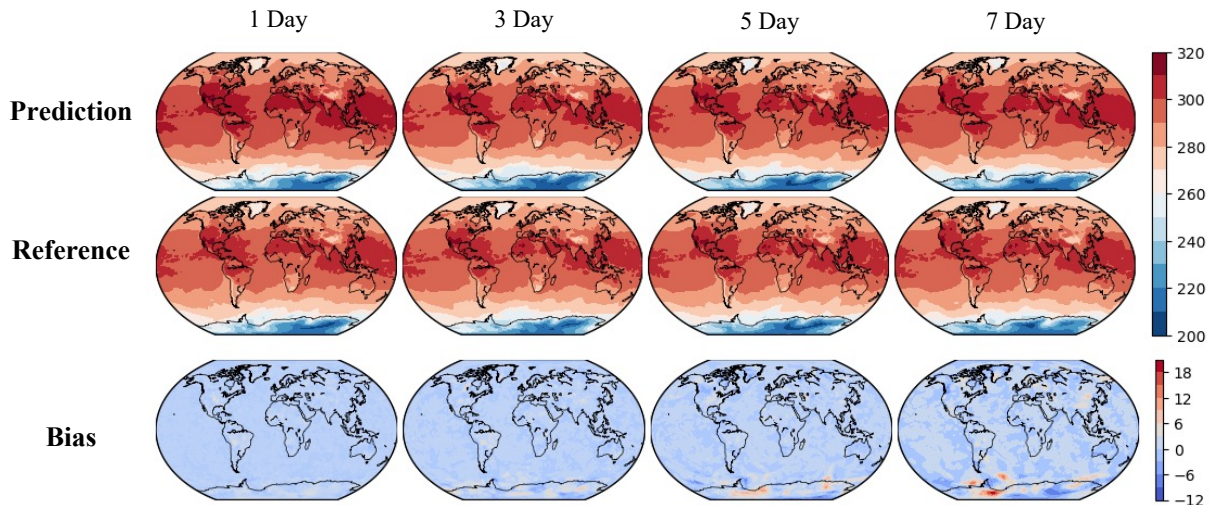
Figure 4.3: Comparison of CaFA and NWP in specific humidity and wind velocity prediction of year 2020.

| Variables | z500 [kg ² /m ²] | | | | t850 [K] | | | | t2m [K] | | | | u10m [m/s] | | | | TFLOPs |
|-------------|---|-----|-----|-----|----------|------|------|------|---------|------|------|------|------------|------|------|------|--------|
| | 24 | 72 | 120 | 168 | 24 | 72 | 120 | 168 | 24 | 72 | 120 | 168 | 24 | 72 | 120 | 168 | |
| CaFA*(Ours) | 51 | 170 | 348 | 544 | 0.59 | 1.04 | 1.71 | 2.47 | 0.49 | 0.82 | 1.28 | 1.79 | 0.58 | 1.28 | 2.15 | 2.97 | 0.61 |
| ClimaX-AR | 71 | 215 | 404 | 585 | 0.73 | 1.25 | 1.93 | 2.62 | 0.56 | 0.95 | 1.42 | 1.90 | 0.69 | 1.50 | 2.37 | 3.08 | 2.22 |
| ClimaX* | 96 | 244 | 440 | 599 | 1.11 | 1.59 | 2.23 | 2.77 | 1.10 | 1.43 | 1.83 | 2.18 | 1.41 | 2.18 | 2.94 | 3.43 | - |

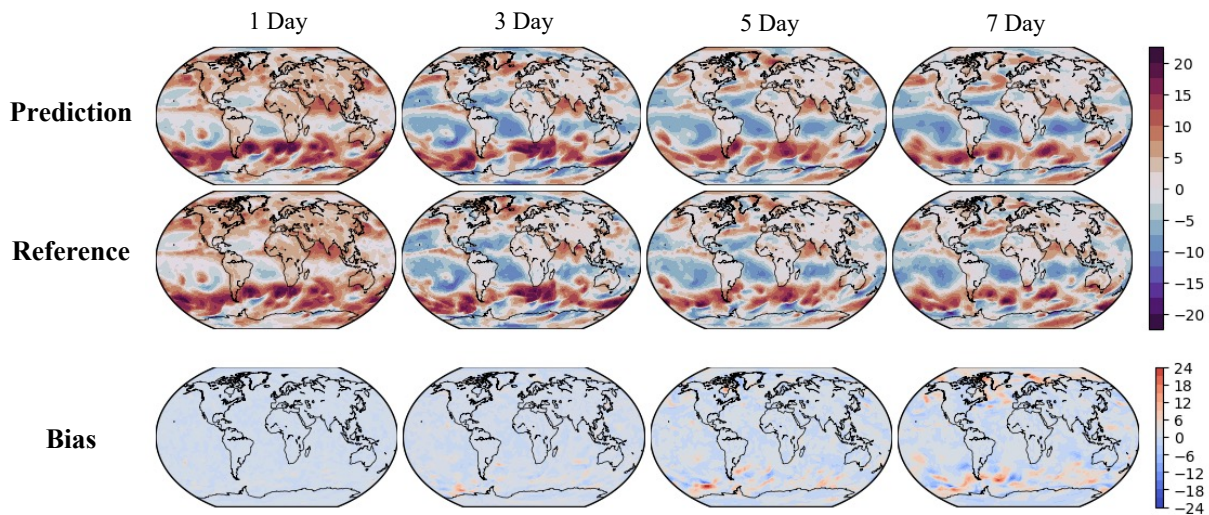
Table 4.4: Comparison of accuracy and computational cost against ClimaX (Nguyen et al., 2023a) on a 5.625° resolution grid. The data splitting follows the strategy used in ClimaX, where the test years are 2017, 2018. ClimaX* is the direct prediction model reported in the original paper (Table 10) and uses fewer atmospheric variables than our framework. T (tera) FLOPs (number of floating point operations) of models’ forward propagation is measured using the DeepSpeed profiling utility (Rasley et al., 2020) with PyTorch 2.1 and a batch size of 8. CaFA* is a smaller version of the major model, with a processor hidden dimension of 512 (2/3 of the number specified in Table 3.1) and the total trainable amount of parameters therefore roughly matches ClimaX (~100M). The number of attention heads is 16 for both ClimaX and CaFA, while the hidden dimension of each attention head is 128 for CaFA and 64 for ClimaX.



(a) z500 example rollout visualization



(b) t_{2m} example rollout visualization



(c) u_{10m} example rollout visualization

Figure 4.4: Example rollout visualizations of the model’s prediction versus reference ERA5 reanalysis data at different lead times. The initialization time is 00:00 UTC on August 11, 2020.

5 Conclusion

In this work we propose an end-to-end machine learning weather prediction model based on factorized attention on a sphere. Our work presents a computationally efficient methodology for computing a data-controlled attention kernel that is capable of capturing long-range dependencies in the domain. The factorized axial kernels only have a single-dimensional domain and thus their computation is very efficient. The proposed attention mechanism respects the underlying periodic boundary along longitudinal direction and responds smoothly with respect to the angular distance between spatial points. Our work signifies an advancement in enhancing the efficiency and accuracy of Transformer-based weather prediction models.

Due to the limited computational budget, the finest resolution we have studied in this work is a spatial resolution of 1.5° and temporal resolution of 6 hours. Scaling the model to higher resolutions in both space and time can potentially allow the model to capture finer scale physics and provide better predictions. In

parallel, it is interesting to study the scaling of model itself to test how much accuracy improvement can be achieved by using more compute. In addition, we have only explored using factorized attention to model spatial interactions, which works particularly well for physical processes that have a decaying spectrum such as geopotential. To further improve the learning capability of higher-frequency components, it is also an interesting direction to combine the proposed model with other localized operators such as message passing around local neighborhoods.

In the current study, we only focus on investigating the short to medium range deterministic forecast capability of the proposed model. However, due to the chaotic nature of weather dynamics, deterministic and purely data-driven models tend to generate blurry predictions in the long run as a result of increasing uncertainty. The IFS ensemble prediction is generally observed to have superior accuracy in longer range forecasting compared to deterministic MLWP. We anticipate that the integration of probabilistic frameworks and ensemble prediction that accounts for the inherent uncertainty will be an important next step. It is also worth pointing out the current model is a purely data-driven approach and it is not guaranteed to satisfy physics constraints. Hence, incorporating more physics priors and symmetries into the model can also be a meaningful future direction.

References

- J. L. Ba, J. R. Kiros, and G. E. Hinton. Layer normalization. *arXiv preprint arXiv:1607.06450*, 2016.
- D. Bahdanau, K. Cho, and Y. Bengio. Neural machine translation by jointly learning to align and translate. In Y. Bengio and Y. LeCun, editors, *3rd International Conference on Learning Representations, ICLR 2015, San Diego, CA, USA, May 7-9, 2015, Conference Track Proceedings*, 2015. URL <http://arxiv.org/abs/1409.0473>.
- P. Bauer, A. J. Thorpe, and G. Brunet. The quiet revolution of numerical weather prediction. *Nature*, 525: 47–55, 2015. URL <https://api.semanticscholar.org/CorpusID:4451289>.
- P. Bauer, T. Quintino, N. Wedi, A. Bonanni, M. Chrust, W. Deconinck, M. Diamantakis, P. Düben, S. English, J. Flemming, P. Gillies, I. Hadade, J. Hawkes, M. Hawkins, O. Iffrig, C. Kühnlein, M. Lange, P. Lean, O. Marsden, A. Müller, S. Saarinen, D. Sarmany, M. Sleigh, S. Smart, P. Smolarkiewicz, D. Thiemert, G. Tumolo, C. Weihrauch, C. Zanna, and P. Maciel. The ecmwf scalability programme: Progress and plans, 02/2020 2020. URL <https://www.ecmwf.int/node/19380>.
- I. Beltagy, M. E. Peters, and A. Cohan. Longformer: The long-document transformer. *arXiv preprint arXiv:2004.05150*, 2020.
- S. G. Benjamin, J. M. Brown, G. Brunet, P. Lynch, K. Saito, and T. W. Schlatter. 100 years of progress in forecasting and nwp applications. *Meteorological Monographs*, 59:13.1 – 13.67, 2018. doi: 10.1175/AMSMONOGRAPH5-D-18-0020.1. URL <https://journals.ametsoc.org/view/journals/amsm/59/1/amsmonographs-d-18-0020.1.xml>.
- K. Bi, L. Xie, H. Zhang, X. Chen, X. Gu, and Q. Tian. Accurate medium-range global weather forecasting with 3d neural networks. *Nature*, 619(7970):533–538, 2023.
- M. Bonavita. On some limitations of data-driven weather forecasting models, 2023.
- B. Bonev, T. Kurth, C. Hundt, J. Pathak, M. Baust, K. Kashinath, and A. Anandkumar. Spherical Fourier neural operators: Learning stable dynamics on the sphere. In A. Krause, E. Brunskill, K. Cho, B. Engelhardt, S. Sabato, and J. Scarlett, editors, *Proceedings of the 40th International Conference on Machine Learning*, volume 202 of *Proceedings of Machine Learning Research*, pages 2806–2823. PMLR, 23–29 Jul 2023. URL <https://proceedings.mlr.press/v202/bonev23a.html>.
- T. Brown, B. Mann, N. Ryder, M. Subbiah, J. D. Kaplan, P. Dhariwal, A. Neelakantan, P. Shyam, G. Sastry, A. Askell, S. Agarwal, A. Herbert-Voss, G. Krueger, T. Henighan, R. Child, A. Ramesh, D. Ziegler, J. Wu, C. Winter, C. Hesse, M. Chen, E. Sigler, M. Litwin, S. Gray, B. Chess, J. Clark, C. Berner, S. McCandlish, A. Radford, I. Sutskever, and D. Amodei. Language models are few-shot learners. In H. Larochelle,

- M. Ranzato, R. Hadsell, M. Balcan, and H. Lin, editors, *Advances in Neural Information Processing Systems*, volume 33, pages 1877–1901. Curran Associates, Inc., 2020. URL https://proceedings.neurips.cc/paper_files/paper/2020/file/1457c0d6bfc4967418bfb8ac142f64a-Paper.pdf.
- S. Cao. Choose a transformer: Fourier or galerkin. In A. Beygelzimer, Y. Dauphin, P. Liang, and J. W. Vaughan, editors, *Advances in Neural Information Processing Systems*, 2021. URL <https://openreview.net/forum?id=ssohLcmn4-r>.
- K. Chen, T. Han, J. Gong, L. Bai, F. Ling, J.-J. Luo, X. Chen, L. Ma, T. Zhang, R. Su, et al. Fengwu: Pushing the skillful global medium-range weather forecast beyond 10 days lead. *arXiv preprint arXiv:2304.02948*, 2023a.
- L. Chen, F. Du, Y. Hu, Z. Wang, and F. Wang. Swinrdm: integrate swinrrn with diffusion model towards high-resolution and high-quality weather forecasting. In *Proceedings of the AAAI Conference on Artificial Intelligence*, volume 37, pages 322–330, 2023b.
- L. Chen, X. Zhong, F. Zhang, Y. Cheng, Y. Xu, Y. Qi, and H. Li. Fuxi: a cascade machine learning forecasting system for 15-day global weather forecast. *npj Climate and Atmospheric Science*, 6(1):190, 2023c.
- K. M. Choromanski, V. Likhoshesterov, D. Dohan, X. Song, A. Gane, T. Sarlos, P. Hawkins, J. Q. Davis, A. Mohiuddin, L. Kaiser, et al. Rethinking attention with performers. In *International Conference on Learning Representations*, 2020.
- T. Dao, D. Fu, S. Ermon, A. Rudra, and C. Ré. Flashattention: Fast and memory-efficient exact attention with io-awareness. *Advances in Neural Information Processing Systems*, 35:16344–16359, 2022.
- J. Devlin, M.-W. Chang, K. Lee, and K. Toutanova. BERT: Pre-training of deep bidirectional transformers for language understanding. In J. Burstein, C. Doran, and T. Solorio, editors, *Proceedings of the 2019 Conference of the North American Chapter of the Association for Computational Linguistics: Human Language Technologies, Volume 1 (Long and Short Papers)*, pages 4171–4186, Minneapolis, Minnesota, June 2019. Association for Computational Linguistics. doi: 10.18653/v1/N19-1423. URL <https://aclanthology.org/N19-1423>.
- A. Dosovitskiy, L. Beyer, A. Kolesnikov, D. Weissenborn, X. Zhai, T. Unterthiner, M. Dehghani, M. Minderer, G. Heigold, S. Gelly, J. Uszkoreit, and N. Houlsby. An image is worth 16x16 words: Transformers for image recognition at scale. In *International Conference on Learning Representations*, 2021. URL <https://openreview.net/forum?id=YicbFdNTTy>.
- P. D. Dueben and P. Bauer. Challenges and design choices for global weather and climate models based on machine learning. *Geosci. Model Dev.*, 2018. doi: 10.5194/gmd-2018-148. URL <https://www.geosci-model-dev-discuss.net/gmd-2018-148/gmd-2018-148.pdf>.
- A. A. A. Elhag, Y. Wang, J. M. Susskind, and M. Á. Bautista. Manifold diffusion fields. In *The Twelfth International Conference on Learning Representations*, 2024. URL <https://openreview.net/forum?id=BZtEthuXRF>.
- D. J. Gagne, A. McGovern, and M. Xue. Machine learning enhancement of storm-scale ensemble probabilistic quantitative precipitation forecasts. *Weather and Forecasting*, 29(4):1024 – 1043, 2014. doi: 10.1175/WAF-D-13-00108.1. URL https://journals.ametsoc.org/view/journals/wefo/29/4/waf-d-13-00108_1.xml.
- J. Gasteiger, J. Groß, and S. Günnemann. Directional message passing for molecular graphs. In *International Conference on Learning Representations*, 2019.
- J. Gasteiger, F. Becker, and S. Günnemann. Gemnet: Universal directional graph neural networks for molecules. *Advances in Neural Information Processing Systems*, 34:6790–6802, 2021.
- J. Guibas, M. Mardani, Z. Li, A. Tao, A. Anandkumar, and B. Catanzaro. Efficient token mixing for transformers via adaptive fourier neural operators. In *International Conference on Learning Representations*, 2022. URL <https://openreview.net/forum?id=EXHG-A3jlm>.

- R. Guo, S. Cao, and L. Chen. Transformer meets boundary value inverse problems. In *The Eleventh International Conference on Learning Representations*, 2023. URL <https://openreview.net/forum?id=Hn1CZATopvr>.
- Z. Hao, Z. Wang, H. Su, C. Ying, Y. Dong, S. Liu, Z. Cheng, J. Song, and J. Zhu. Gnot: A general neural operator transformer for operator learning. In *International Conference on Machine Learning*, pages 12556–12569. PMLR, 2023.
- K. He, X. Zhang, S. Ren, and J. Sun. Deep residual learning for image recognition. In *Proceedings of the IEEE conference on computer vision and pattern recognition*, pages 770–778, 2016.
- A. Hemmasian and A. Barati Farimani. Reduced-order modeling of fluid flows with transformers. *Physics of Fluids*, 35(5):057126, 05 2023. ISSN 1070-6631. doi: 10.1063/5.0151515. URL <https://doi.org/10.1063/5.0151515>.
- D. Hendrycks and K. Gimpel. Gaussian error linear units (gelus), 2023.
- H. Hersbach, B. Bell, P. Berrisford, S. Hirahara, A. Horányi, J. Muñoz-Sabater, J. Nicolas, C. Peubey, R. Radu, D. Schepers, A. Simmons, C. Soci, S. Abdalla, X. Abellan, G. Balsamo, P. Bechtold, G. Biavati, J. Bidlot, M. Bonavita, G. De Chiara, P. Dahlgren, D. Dee, M. Diamantakis, R. Dragani, J. Flemming, R. Forbes, M. Fuentes, A. Geer, L. Haimberger, S. Healy, R. J. Hogan, E. Hólm, M. Janisková, S. Keeley, P. Laloyaux, P. Lopez, C. Lupu, G. Radnoti, P. de Rosnay, I. Rozum, F. Vamborg, S. Villaume, and J.-N. Thépaut. The era5 global reanalysis. *Quarterly Journal of the Royal Meteorological Society*, 146(730):1999–2049, 2020. doi: <https://doi.org/10.1002/qj.3803>. URL <https://rmets.onlinelibrary.wiley.com/doi/abs/10.1002/qj.3803>.
- J. Ho, N. Kalchbrenner, D. Weissenborn, and T. Salimans. Axial attention in multidimensional transformers, 2020. URL <https://openreview.net/forum?id=H1e5GJBtDr>.
- J. W. Hurrell, M. M. Holland, P. R. Gent, S. Ghan, J. E. Kay, P. J. Kushner, J.-F. Lamarque, W. G. Large, D. Lawrence, K. Lindsay, W. H. Lipscomb, M. C. Long, N. Mahowald, D. R. Marsh, R. B. Neale, P. Rasch, S. Vavrus, M. Vertenstein, D. Bader, W. D. Collins, J. J. Hack, J. Kiehl, and S. Marshall. The community earth system model: A framework for collaborative research. *Bulletin of the American Meteorological Society*, 94(9):1339 – 1360, 2013. doi: 10.1175/BAMS-D-12-00121.1. URL <https://journals.ametsoc.org/view/journals/bams/94/9/bams-d-12-00121.1.xml>.
- J. Jumper, R. Evans, A. Pritzel, T. Green, M. Figurnov, O. Ronneberger, K. Tunyasuvunakool, R. Bates, A. Žídek, A. Potapenko, et al. Highly accurate protein structure prediction with alphafold. *Nature*, 596(7873):583–589, 2021.
- R. Keisler. Forecasting global weather with graph neural networks. *arXiv preprint arXiv:2202.07575*, 2022.
- D. Kingma and J. Ba. Adam: A method for stochastic optimization. In *International Conference on Learning Representations (ICLR)*, San Diego, CA, USA, 2015.
- G. Kissas, J. H. Seidman, L. F. Guilhoto, V. M. Preciado, G. J. Pappas, and P. Perdikaris. Learning operators with coupled attention. *Journal of Machine Learning Research*, 23(215):1–63, 2022.
- D. Kochkov, J. Yuval, I. Langmore, P. Norgaard, J. Smith, G. Mooers, J. Lottes, S. Rasp, P. Düben, M. Klöwer, et al. Neural general circulation models. *arXiv preprint arXiv:2311.07222*, 2023.
- N. Kovachki, Z. Li, B. Liu, K. Azizzadenesheli, K. Bhattacharya, A. Stuart, and A. Anandkumar. Neural operator: Learning maps between function spaces with applications to pdes. *Journal of Machine Learning Research*, 24(89):1–97, 2023.
- T. Kurth, S. Subramanian, P. Harrington, J. Pathak, M. Mardani, D. Hall, A. Miele, K. Kashinath, and A. Anandkumar. Fourcastnet: Accelerating global high-resolution weather forecasting using adaptive fourier neural operators. In *Proceedings of the platform for advanced scientific computing conference*, pages 1–11, 2023.

- R. Lagerquist, A. McGovern, and T. Smith. Machine learning for real-time prediction of damaging straight-line convective wind. *Weather and Forecasting*, 32(6):2175–2193, 12 2017. ISSN 15200434. doi: 10.1175/WAF-D-17-0038.1.
- R. Lam, A. Sanchez-Gonzalez, M. Willson, P. Wirnsberger, M. Fortunato, F. Alet, S. Ravuri, T. Ewalds, Z. Eaton-Rosen, W. Hu, et al. Learning skillful medium-range global weather forecasting. *Science*, 382(6677):1416–1421, 2023.
- G. Larsson, M. Maire, and G. Shakhnarovich. Fractalnet: Ultra-deep neural networks without residuals. In *International Conference on Learning Representations*, 2016.
- D. A. Lavers, A. Simmons, F. Vamborg, and M. J. Rodwell. An evaluation of era5 precipitation for climate monitoring. *Quarterly Journal of the Royal Meteorological Society*, 148(748):3152–3165, 2022. doi: <https://doi.org/10.1002/qj.4351>. URL <https://rmets.onlinelibrary.wiley.com/doi/abs/10.1002/qj.4351>.
- J. Leinonen, D. Nerini, and A. Berne. Stochastic super-resolution for downscaling time-evolving atmospheric fields with a generative adversarial network. *IEEE Transactions on Geoscience and Remote Sensing*, 59(9):7211–7223, 2021. doi: 10.1109/TGRS.2020.3032790.
- J. Leinonen, U. Hamann, D. Nerini, U. Germann, and G. Franch. Latent diffusion models for generative precipitation nowcasting with accurate uncertainty quantification. *arXiv preprint arXiv:2304.12891*, 2023.
- L. Li, R. Carver, I. Lopez-Gomez, F. Sha, and J. Anderson. Seeds: Emulation of weather forecast ensembles with diffusion models. *arXiv preprint arXiv:2306.14066*, 2023a.
- Z. Li, N. B. Kovachki, K. Azizzadenesheli, B. liu, K. Bhattacharya, A. Stuart, and A. Anandkumar. Fourier neural operator for parametric partial differential equations. In *International Conference on Learning Representations*, 2021. URL <https://openreview.net/forum?id=c8P9NQVtm0>.
- Z. Li, K. Meidani, and A. B. Farimani. Transformer for partial differential equations’ operator learning. *Transactions on Machine Learning Research*, 2023b. ISSN 2835-8856. URL <https://openreview.net/forum?id=EPPqt3uERT>.
- Z. Li, D. Shu, and A. Barati Farimani. Scalable transformer for pde surrogate modeling. *Advances in Neural Information Processing Systems*, 36, 2024.
- X. Liu, B. Xu, S. Cao, and L. Zhang. Mitigating spectral bias for the multiscale operator learning. *Journal of Computational Physics*, 506:112944, 2024. ISSN 0021-9991. doi: <https://doi.org/10.1016/j.jcp.2024.112944>. URL <https://www.sciencedirect.com/science/article/pii/S0021999124001931>.
- Z. Liu, Y. Lin, Y. Cao, H. Hu, Y. Wei, Z. Zhang, S. Lin, and B. Guo. Swin transformer: Hierarchical vision transformer using shifted windows. In *Proceedings of the IEEE/CVF international conference on computer vision*, pages 10012–10022, 2021.
- I. Loshchilov and F. Hutter. Decoupled weight decay regularization. In *International Conference on Learning Representations*, 2019. URL <https://openreview.net/forum?id=Bkg6RiCqY7>.
- P. Lynch. The origins of computer weather prediction and climate modeling. *Journal of Computational Physics*, 227(7):3431–3444, 2008. ISSN 0021-9991. doi: <https://doi.org/10.1016/j.jcp.2007.02.034>. URL <https://www.sciencedirect.com/science/article/pii/S0021999107000952>. Predicting weather, climate and extreme events.
- M. Mardani, N. Brenowitz, Y. Cohen, J. Pathak, C.-Y. Chen, C.-C. Liu, A. Vahdat, K. Kashinath, J. Kautz, and M. Pritchard. Generative residual diffusion modeling for km-scale atmospheric downscaling. *arXiv preprint arXiv:2309.15214*, 2023.
- B. Mildenhall, P. P. Srinivasan, M. Tancik, J. T. Barron, R. Ramamoorthi, and R. Ng. Nerf: Representing scenes as neural radiance fields for view synthesis. In *European Conference on Computer Vision*, pages 405–421. Springer, 2020.

- P. Nath, P. Shukla, and C. Quilodr an-Casas. Forecasting tropical cyclones with cascaded diffusion models. *arXiv preprint arXiv:2310.01690*, 2023.
- T. Nguyen, J. Brandstetter, A. Kapoor, J. K. Gupta, and A. Grover. ClimaX: A foundation model for weather and climate. In A. Krause, E. Brunskill, K. Cho, B. Engelhardt, S. Sabato, and J. Scarlett, editors, *Proceedings of the 40th International Conference on Machine Learning*, volume 202 of *Proceedings of Machine Learning Research*, pages 25904–25938. PMLR, 23–29 Jul 2023a. URL <https://proceedings.mlr.press/v202/nguyen23a.html>.
- T. Nguyen, R. Shah, H. Bansal, T. Arcomano, S. Madireddy, R. Maulik, V. Kotamarthi, I. Foster, and A. Grover. Scaling transformer neural networks for skillful and reliable medium-range weather forecasting. *arXiv preprint arXiv:2312.03876*, 2023b.
- A. Paszke, S. Gross, F. Massa, A. Lerer, J. Bradbury, G. Chanan, T. Killeen, Z. Lin, N. Gimelshein, L. Antiga, et al. Pytorch: An imperative style, high-performance deep learning library. *Advances in neural information processing systems*, 32, 2019.
- E. Perez, F. Strub, H. De Vries, V. Dumoulin, and A. Courville. Film: Visual reasoning with a general conditioning layer. In *Proceedings of the AAAI conference on artificial intelligence*, volume 32, 2018.
- N. A. Phillips. The general circulation of the atmosphere: A numerical experiment. *Quarterly Journal of the Royal Meteorological Society*, 82(354):535–539, Oct. 1956. doi: 10.1002/qj.49708235422.
- I. Price, A. Sanchez-Gonzalez, F. Alet, T. Ewalds, A. El-Kadi, J. Stott, S. Mohamed, P. Battaglia, R. Lam, and M. Willson. Gencast: Diffusion-based ensemble forecasting for medium-range weather. *arXiv preprint arXiv:2312.15796*, 2023.
- M. N. Rabe and C. Staats. Self-attention does not need $o(n^2)$ memory. *arXiv preprint arXiv:2112.05682*, 2021.
- J. Rasley, S. Rajbhandari, O. Ruwase, and Y. He. Deepspeed: System optimizations enable training deep learning models with over 100 billion parameters. In *Proceedings of the 26th ACM SIGKDD International Conference on Knowledge Discovery & Data Mining*, KDD ’20, page 3505–3506, New York, NY, USA, 2020. Association for Computing Machinery. ISBN 9781450379984. doi: 10.1145/3394486.3406703. URL <https://doi.org/10.1145/3394486.3406703>.
- S. Rasp and N. Thuerey. Data-driven medium-range weather prediction with a resnet pretrained on climate simulations: A new model for weatherbench. *Journal of Advances in Modeling Earth Systems*, 13(2):e2020MS002405, 2021. doi: <https://doi.org/10.1029/2020MS002405>. URL <https://agupubs.onlinelibrary.wiley.com/doi/abs/10.1029/2020MS002405>. e2020MS002405 2020MS002405.
- S. Rasp, M. S. Pritchard, and P. Gentine. Deep learning to represent subgrid processes in climate models. *Proceedings of the National Academy of Sciences*, 115(39):9684–9689, 2018. doi: 10.1073/pnas.1810286115. URL <https://www.pnas.org/doi/abs/10.1073/pnas.1810286115>.
- S. Rasp, S. Hoyer, A. Merose, I. Langmore, P. Battaglia, T. Russel, A. Sanchez-Gonzalez, V. Yang, R. Carver, S. Agrawal, M. Chantry, Z. B. Bouallegue, P. Dueben, C. Bromberg, J. Sisk, L. Barrington, A. Bell, and F. Sha. Weatherbench 2: A benchmark for the next generation of data-driven global weather models, 2023.
- M. Ru wurm, K. Klemmer, E. Rolf, R. Zbinden, and D. Tuia. Geographic location encoding with spherical harmonics and sinusoidal representation networks. In *The Twelfth International Conference on Learning Representations*, 2024. URL <https://openreview.net/forum?id=PudduufFLa>.
- A. Sanchez-Gonzalez, J. Godwin, T. Pfaff, R. Ying, J. Leskovec, and P. Battaglia. Learning to simulate complex physics with graph networks. In *International conference on machine learning*, pages 8459–8468. PMLR, 2020.
- M. Satoh. *Atmospheric circulation dynamics and general circulation models*. Springer Science & Business Media, 2013.

- S. Scher. Toward data-driven weather and climate forecasting: Approximating a simple general circulation model with deep learning. *Geophysical Research Letters*, 45(22):12,616–12,622, 2018. doi: <https://doi.org/10.1029/2018GL080704>. URL <https://agupubs.onlinelibrary.wiley.com/doi/abs/10.1029/2018GL080704>.
- S. Scher and G. Messori. Generalization properties of neural networks trained on Lorenzsystems. *Nonlinear Processes in Geophysics Discussions*, pages 1–19, 6 2019. ISSN 2198-5634. doi: 10.5194/npg-2019-23. URL <https://www.nonlin-processes-geophys-discuss.net/npg-2019-23/>.
- S. C. Sherwood, S. Bony, and J.-L. Dufresne. Spread in model climate sensitivity traced to atmospheric convective mixing. *Nature*, 505(7481):37–42, 2014.
- V. Sitzmann, J. Martel, A. Bergman, D. Lindell, and G. Wetzstein. Implicit neural representations with periodic activation functions. *Advances in neural information processing systems*, 33:7462–7473, 2020.
- C. K. S nderby, L. Espenholt, J. Heek, M. Dehghani, A. Oliver, T. Salimans, S. Agrawal, J. Hickey, and N. Kalchbrenner. Metnet: A neural weather model for precipitation forecasting. *arXiv preprint arXiv:2003.12140*, 2020.
- N. Srivastava, G. Hinton, A. Krizhevsky, I. Sutskever, and R. Salakhutdinov. Dropout: A simple way to prevent neural networks from overfitting. *Journal of Machine Learning Research*, 15(56):1929–1958, 2014. URL <http://jmlr.org/papers/v15/srivastava14a.html>.
- D. J. Stensrud. *Parameterization Schemes: Keys to Understanding Numerical Weather Prediction Models*. Cambridge University Press, 2007.
- J. Su, M. Ahmed, Y. Lu, S. Pan, W. Bo, and Y. Liu. Roformer: Enhanced transformer with rotary position embedding. *Neurocomputing*, 568:127063, 2024.
- A. Vaswani, N. Shazeer, N. Parmar, J. Uszkoreit, L. Jones, A. N. Gomez, L. u. Kaiser, and I. Polosukhin. Attention is all you need. In I. Guyon, U. V. Luxburg, S. Bengio, H. Wallach, R. Fergus, S. Vishwanathan, and R. Garnett, editors, *Advances in Neural Information Processing Systems*, volume 30. Curran Associates, Inc., 2017. URL https://proceedings.neurips.cc/paper_files/paper/2017/file/3f5ee243547dee91fbd053c1c4a845aa-Paper.pdf.
- Y. Verma, M. Heinonen, and V. Garg. ClimODE: Climate and weather forecasting with physics-informed neural ODEs. In *The Twelfth International Conference on Learning Representations*, 2024. URL <https://openreview.net/forum?id=xuY33XhEGR>.
- M. J. Webb, F. H. Lambert, and J. M. Gregory. Origins of differences in climate sensitivity, forcing and feedback in climate models. *Climate Dynamics*, 40:677–707, 2013.
- N. Wedi, P. Bauer, W. Denoninck, M. Diamantakis, M. Hamrud, C. Kuhnlein, S. Malardel, K. Mogensen, G. Mozdzyński, and P. Smolarkiewicz. *The modelling infrastructure of the Integrated Forecasting System: Recent advances and future challenges*. European Centre for Medium-Range Weather Forecasts, 2015.
- J. A. Weyn, D. R. Durran, and R. Caruana. Can machines learn to predict weather? Using deep learning to predict gridded 500-hPa geopotential height from historical weather data. *Journal of Advances in Modeling Earth Systems*, page 2019MS001705, 7 2019. ISSN 1942-2466. doi: 10.1029/2019MS001705. URL <https://onlinelibrary.wiley.com/doi/abs/10.1029/2019MS001705>.
- J. A. Weyn, D. R. Durran, and R. Caruana. Improving data-driven global weather prediction using deep convolutional neural networks on a cubed sphere. *Journal of Advances in Modeling Earth Systems*, 12(9):e2020MS002109, 2020.

Supplementary Material

Contents

| | | |
|----------|--|-----------|
| 1 | Introduction | 1 |
| 2 | Related Works | 2 |
| 3 | Methodology | 5 |
| 3.1 | Attention mechanism | 5 |
| 3.2 | Axial factorized attention on sphere | 5 |
| 3.3 | Grid projection | 7 |
| 3.4 | Model overview | 7 |
| 4 | Experiments and Results | 9 |
| 4.1 | Evaluation setting | 9 |
| 4.2 | Discussion | 9 |
| 5 | Conclusion | 13 |
| A | Model implementation | 21 |
| A.1 | Training details | 21 |
| A.2 | Metrics | 22 |
| B | Comparison against standard attention | 23 |
| C | Further results | 25 |

A Model implementation

A.1 Training details

We specify the detailed hyperparameters for the model training in Table A.1 and A.2. We implement the model and the experiment using PyTorch (Paszke et al., 2019). We use AdamW optimizer (Kingma and Ba, 2015; Loshchilov and Hutter, 2019) and the majority of the hyperparameter setting follows ClimaX (Nguyen et al., 2023a). Regularization techniques including dropout (Srivastava et al., 2014) and droppath (Larsson et al., 2016) are not used in the proposed model (which is used in ClimaX baseline). For testing, we evaluate the final model checkpoint and no early stopping is applied. During second-stage training, gradient checkpointing is used to reduce the memory cost of backpropagating through time. In addition, only the most recent 20 years’ (up to the validation years) training data is used for second stage training.

| Training Hyperparameter | Value |
|-------------------------|---|
| Optimizer | AdamW |
| Learning rate | $1e-8 \mapsto 3e-4 \mapsto 1e-7$ |
| Batch size | 8 |
| Gradient steps | 160k |
| Learning rate scheduler | Cosine Annealing with Linear Warmup (for 1600 steps) |
| Weight decay | 1e-6 |
| Rollout step curriculum | [1, 2] |
| Curriculum milestone | [0, 50k] |
| EMA | None |

Table A.1: Training hyperparameter for stage 1. On 64×32 grid we adjust the batch size to 16 and peak learning rate to $5e-4$. The curriculum milestone determines how many steps to rollout after specific milestone. In the above setting, after 50k gradient steps, the model will rollout for 2 steps.

| Training Hyperparameter | Value |
|-------------------------|--|
| Optimizer | AdamW |
| Learning rate | $1e-8 \mapsto 3e-7 \mapsto 1e-7$ |
| Batch size | 8 |
| Gradient steps | 50k |
| Learning rate scheduler | Cosine Annealing with Linear Warmup (for 500 steps) |
| Weight decay | 1e-6 |
| Rollout step curriculum | [4, 8, 12, 16, 20] |
| Curriculum milestone | [0, 10k, 20k, 30k, 40k] |
| EMA | Deacy=0.999 |

Table A.2: Training hyperparameter for stage 2. We save the Exponential Moving Average (EMA) of model weights during the second stage.

The training loss is a latitude-weighted and variable-weighted $L1$ loss:

$$\text{Loss}(\hat{X}, X) = \frac{1}{N_{\text{lat}}N_{\text{lon}}N_t} \sum_{c=1}^{N_c} \lambda_c \sum_{l=1}^{N_{\text{level}}} \lambda_l \sum_{t=1}^{N_t} \sum_{i=1}^{N_{\text{lat}}} \sum_{j=1}^{N_{\text{lon}}} w(i) \|\hat{X}_{tijl}^c - X_{tijl}^c\|, \quad (13)$$

where $w(i)$ is the latitude-based weight (see Equation 12), λ_l is the level-based weight, λ_c is the variable-based weight, \hat{X} is model’s prediction and X is reference data, N_t denotes total number of rollout timesteps, N_{lat} denotes number of latitude grid points, N_{lon} denotes number of longitude grid points. The level-based weight is a simple linear interpolation between 0.05 and 0.065: $\lambda_l = \text{Index}(l)/12 \times 0.015 + 0.050$, where the index of pressure level l ranges from 0 to 12 corresponds to 50hPa to 1000 hPa. We list the specification of the variable-based weight below (see Table 4.1 for the meaning of the variable abbreviation):

| Variable | z | t | u | v | q | t2m | MSLP | u10 | v10 | TP6 | TP24 |
|----------|-----|-----|-----|-----|-----|-----|------|-----|-----|------|------|
| Weight | 1.0 | 1.0 | 0.5 | 0.5 | 0.1 | 1.0 | 0.1 | 0.1 | 0.1 | 0.05 | 0.05 |

Table A.3: Variable-based weight.

We didn’t perform search over the best combination of variable-based weights and level-based weights. We find uniform level-based weights perform almost similar to current level-based weights in preliminary experiments. The variable weights we’ve used is similar to the variable weights used in GraphCast (Lam et al., 2023). Recent work Stormer (Nguyen et al., 2023b) showcase that using variable-based weight is beneficial for variables that are assigned higher loss weight like 2m temperature, geopotential.

A.2 Metrics

The following metrics are defined on a surface variable or a upper-air variable at a specific level.

Root mean squared error (RMSE) The RMSE for time step t is defined as:

$$\text{RMSE}_t(\hat{X}, X) = \sqrt{\frac{1}{N_{\text{lat}}N_{\text{lon}}} \sum_{i=1}^{N_{\text{lat}}} \sum_{j=1}^{N_{\text{lon}}} w(i) (\hat{X}_{tij} - X_{tij})^2}. \quad (14)$$

Anomaly correlation coefficient (ACC) The ACC is defined as the Pearson correlation coefficient of the anomalies with respect to the climatology:

$$\text{Anomaly: } \hat{X}'_{tij} = \hat{X}_{tij} - C_{\tilde{t}ij}, \quad X'_{tij} = \hat{X}_{tij} - C_{\tilde{t}ij}, \quad (15)$$

$$\text{ACC}_t(\hat{X}', X') = \frac{\sum_{i=1}^{N_{\text{lat}}} \sum_{j=1}^{N_{\text{lon}}} w(i) \hat{X}'_{tij} X'_{tij}}{\sqrt{\left(\sum_{i=1}^{N_{\text{lat}}} \sum_{j=1}^{N_{\text{lon}}} w(i) \hat{X}'_{tij}^2\right) \left(\sum_{i=1}^{N_{\text{lat}}} \sum_{j=1}^{N_{\text{lon}}} w(i) X'^2_{tij}\right)}}, \quad (16)$$

where we use the climatology statistics C provided in WeatherBench2 (Rasp et al., 2023) (computed on ERA5 data from 1990 to 2019), \tilde{t} denotes the day of year and time of day of the corresponding time index t .

Bias The bias is defined as the point-wise difference between prediction and ground truth:

$$\text{Bias}_t(\hat{X}, X) = \hat{X}_{tij} - X_{tij}. \quad (17)$$

B Comparison against standard attention

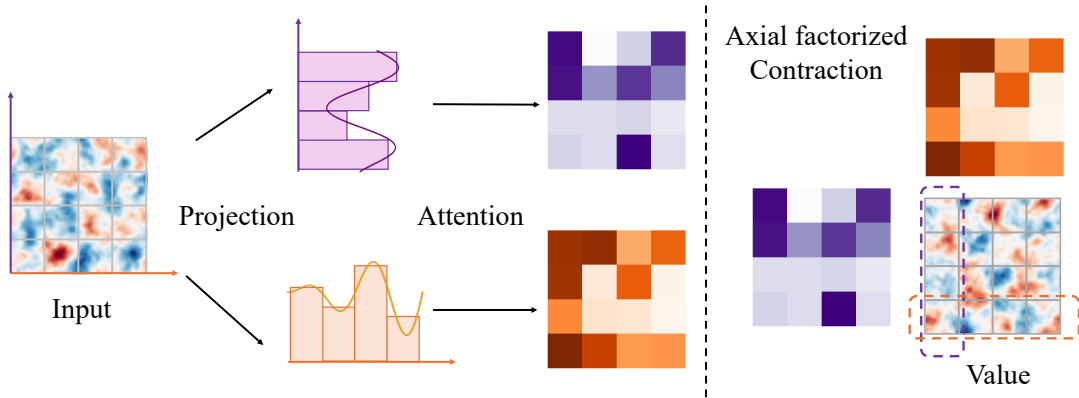


Figure B.1: Axial factorized attention. The multi-dimensional spatial structure of value is preserved, each axial attention kernel matrix’s size is S_m^2 for n -dimensional grid with total size $S = S_1 \times S_2 \times \dots \times S_n$.

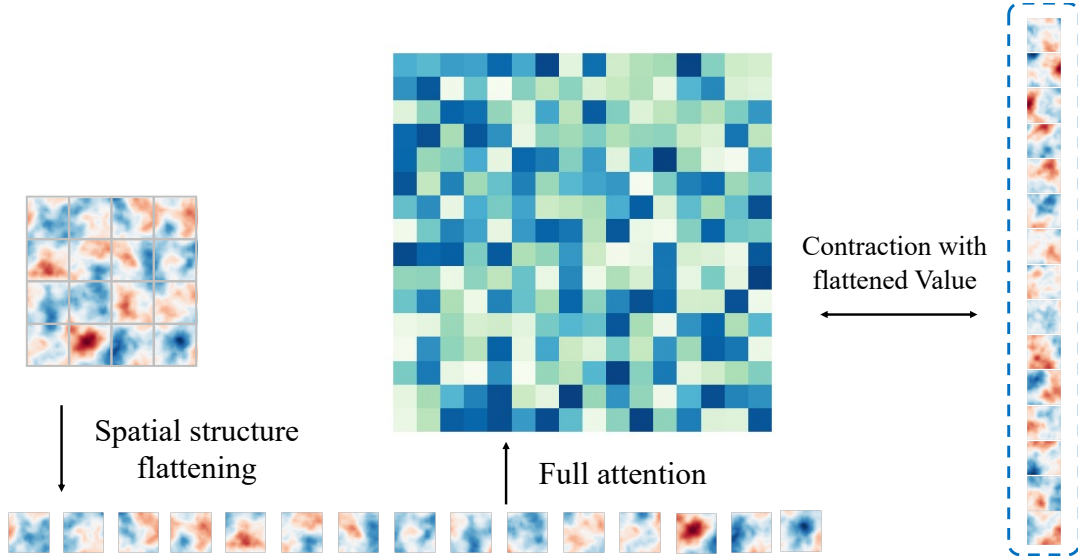


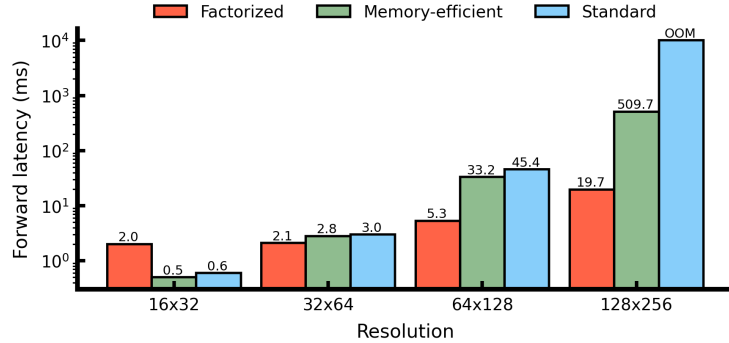
Figure B.2: Standard attention for sequence. The multi-dimensional spatial structure is not considered explicitly during the attention (it can be implicitly encoded via positional encoding). The full attention kernel matrix’s size is quadratic to the total grid size S .

Two illustrative diagrams of factorized attention and standard attention are shown above (Figure B.1 and B.2). In standard attention, the spatial structure is not preserved during the contraction of value and attention kernel. Compared to axial Transformer (Ho et al., 2020), the axial attention kernel in CaFA is still dependent on global information while in axial Transformer its context is limited to that specific row/column.

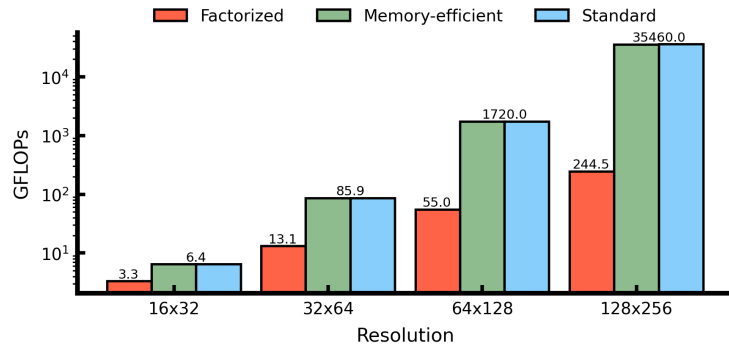
We compare factorized attention to two different implementations of standard attention in PyTorch’s attention function: `torch.nn.functional.scaled_dot_product_attention` - a standard one without memory optimization and another one with memory optimization (Rabe and Staats, 2021)[†]. The results are shown in Figure B.3a, B.3b, B.3c. We observe that factorized attention has significantly better scaling efficiency in terms of runtime and FLOPs. At the lowest resolution, the runtime of factorized attention is larger than

[†]FlashAttention (Dao et al., 2022) is currently not available for `float32` computation on A6000 in PyTorch 2.1.

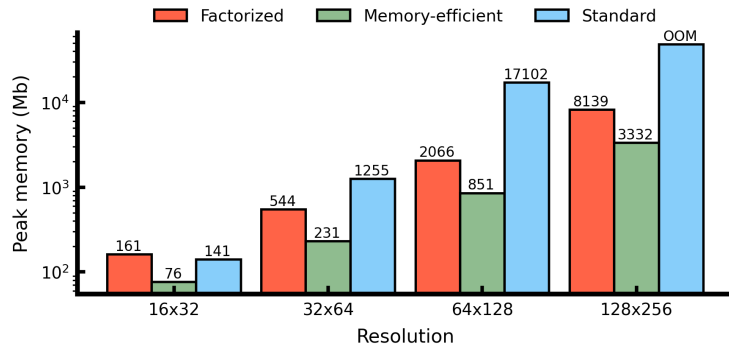
standard attention. This is because in factorized attention layer the input is first processed by two projection layer and then sent to compute the axial attention kernels, with all computation done sequentially [‡]. Compared to memory efficient attention, factorized attention has larger memory footprint at current stage. The memory cost of factorized attention can also be optimized by adopting a similar chunking strategy in [Rabe and Staats \(2021\)](#) during the contraction of value and attention kernels.



(a) Forward latency



(b) Theoretical FLOPs



(c) Peak memory usage

Figure B.3: Computational benchmark between factorized attention and different implementation of the standard softmax attention ([Vaswani et al., 2017](#)). The number of attention head is 16, each attention head’s dimension is 128, batch size is set to 1, input and output channel dimension is 512. The benchmark is carried out on A6000 with CUDA 12, float32 precision is used. The runtime statistics are profiled using DeepSpeed. The factorized attention layer contains following learnable modules that are not in standard attention layer: distance encoding (Equation (10)) and projection layer (Equation (2)).

[‡]For projection and attention kernel’s computation, each axis’s computation are independent to each other and the memory cost is small, so potentially they can be optimized to run in parallel.

C Further results

In this section we provide more quantitative and qualitative analysis of model’s prediction capability.

We analyze how the model perform in terms of $L1$ and $L2$ (RMSE) loss. The normalized difference with respect to IFS HRES is shown in Figure C.1. We observe that the model performs relatively better in terms of $L1$ norm in the long run, which is possibly because that the model is trained on $L1$ norm and penalizes outlier less than $L2$ norm. We also compare models trained with different time step sizes (lead time 6 hour vs 12 hour). We find that model with larger time step size performs better in terms of forecasting accuracy beyond 7 days but performs worse in shorter range, while the ACC of both model variants fall below 0.6 on day 10.

Example visualization of the learned positional encoding, distance encoding and attention kernels are shown in Figure C.3, C.4, C.5. Interestingly, the attention kernel at earlier layer exhibit sharper patterns than deeper layer, where attention scores are mostly concentrated around the diagonal.

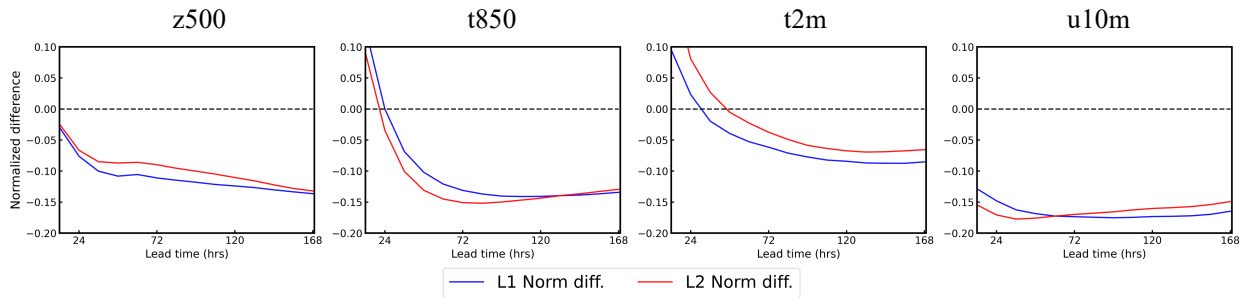


Figure C.1: Relative $L1$ and $L2$ error difference with respect to IFS HRES of 4 selected key variables.

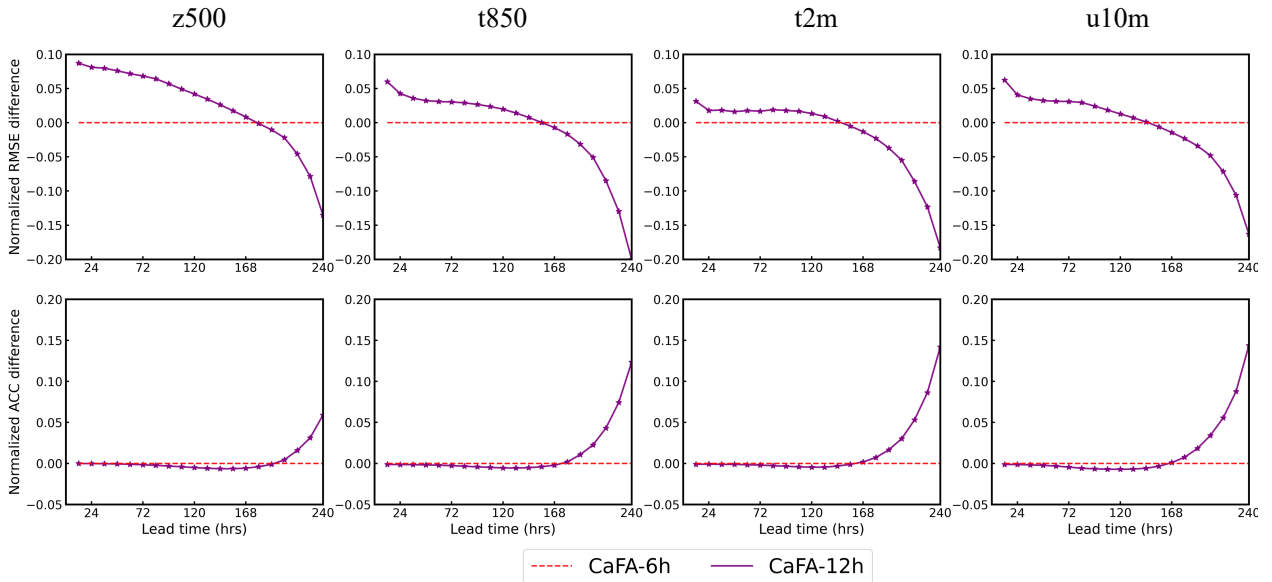


Figure C.2: Normalized RMSE difference and ACC difference comparison between CaFA trained with 6 hour interval and CaFA trained with 12 hour interval. Negative RMSE difference and positive ACC difference indicates better performance. CaFA trained with 12 hour interval uses less gradient steps for the second stage (36k) and fewer rollout steps (up to 16).

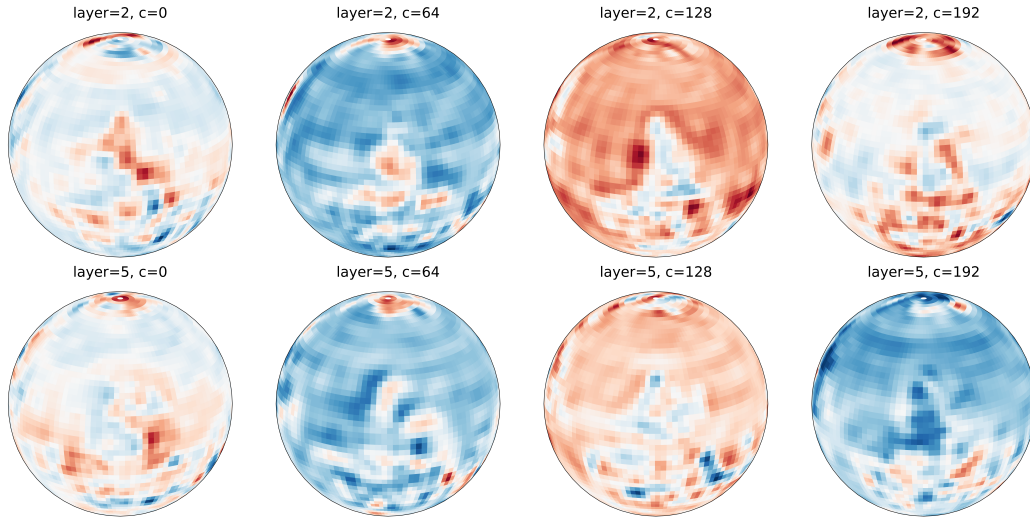


Figure C.3: Example visualization of learned spherical harmonic based positional encoding. "Layer" denotes their corresponding attention layer number, "c" denotes channel number.

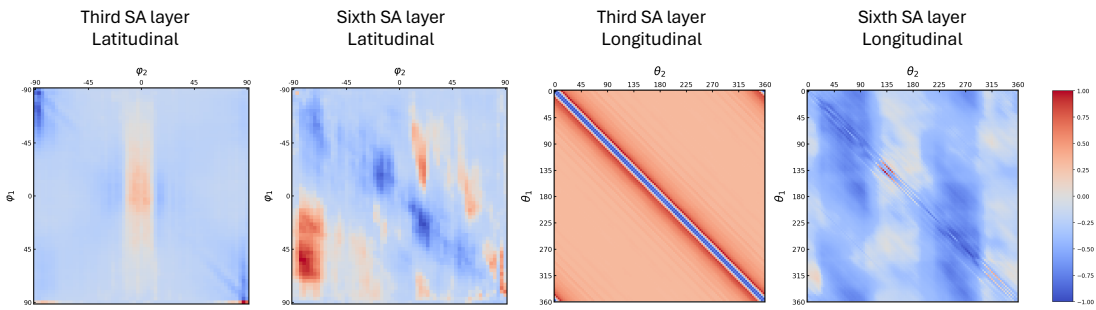


Figure C.4: Example visualization of learned self-attention kernel along different axes. The kernel matrices are selected from random batch and head. For better clarity all the kernel matrices shown are normalized such that all the elements fall into the range of $[-1, 1]$.

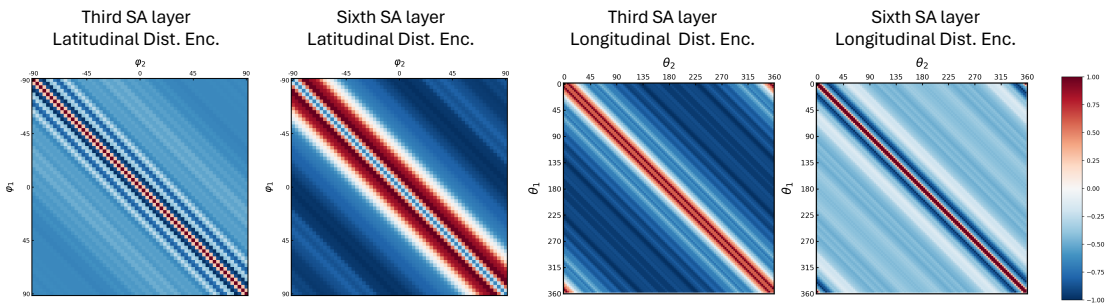
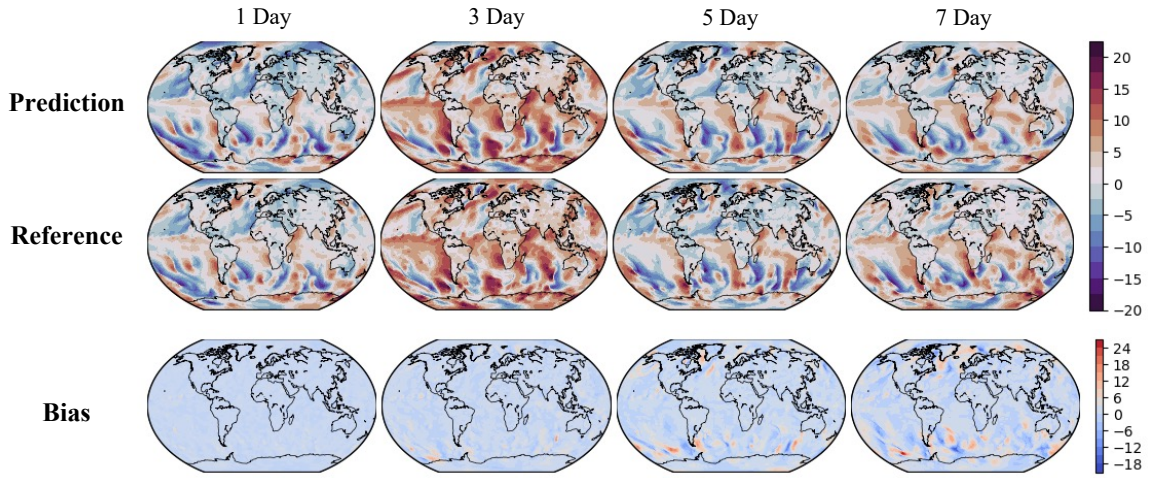
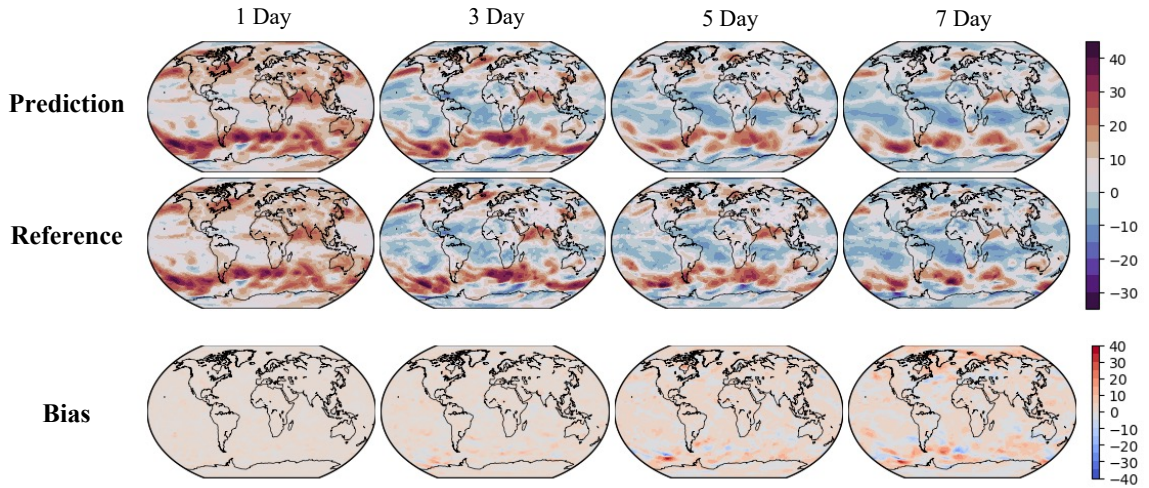


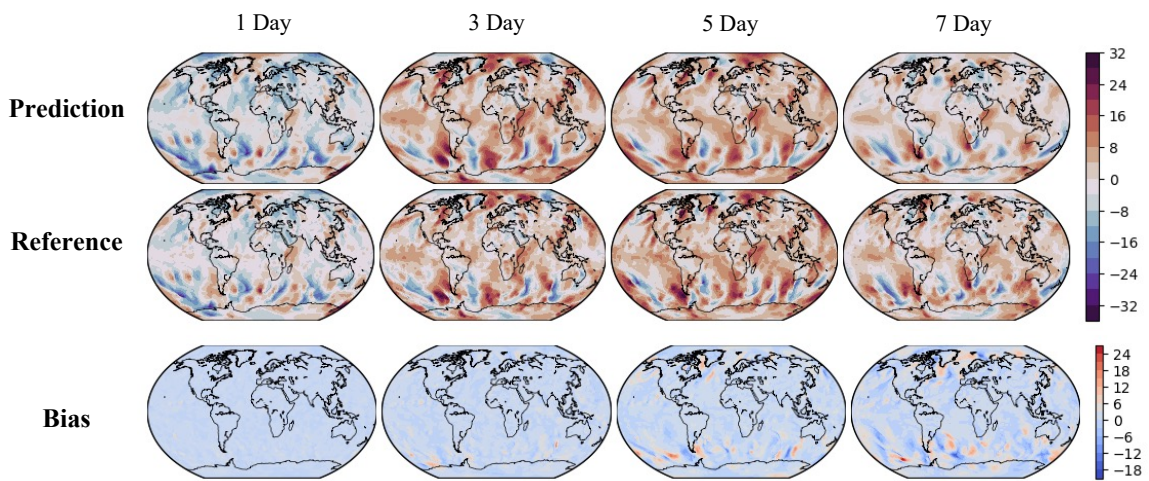
Figure C.5: Example visualization of learned distance encoding along different axes. The distance encoding are selected from random batch, head and channel. For better clarity all the kernel matrices shown are normalized such that all the elements fall into the range of $[-1, 1]$.



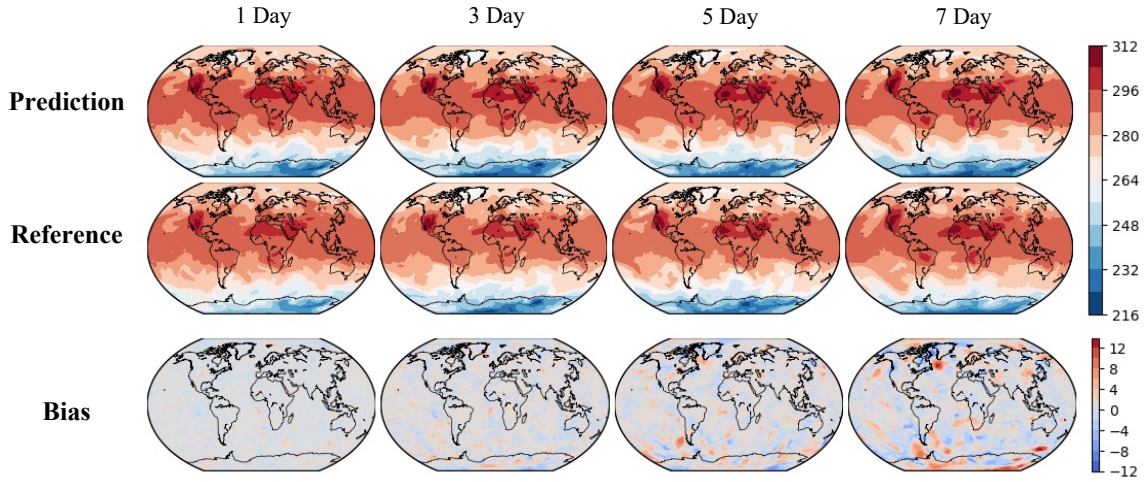
(a) v_{10m} example rollout visualization



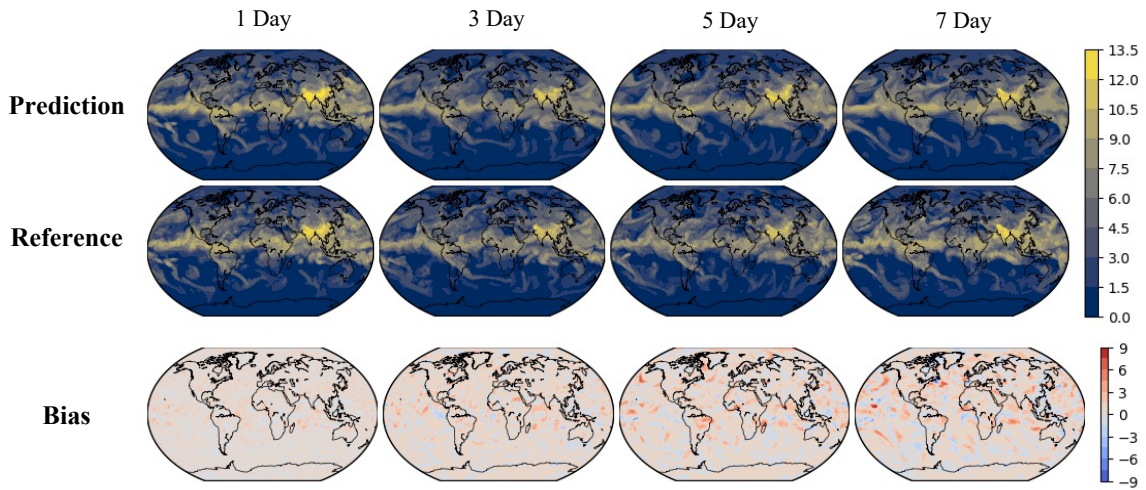
(b) u_{850} example rollout visualization



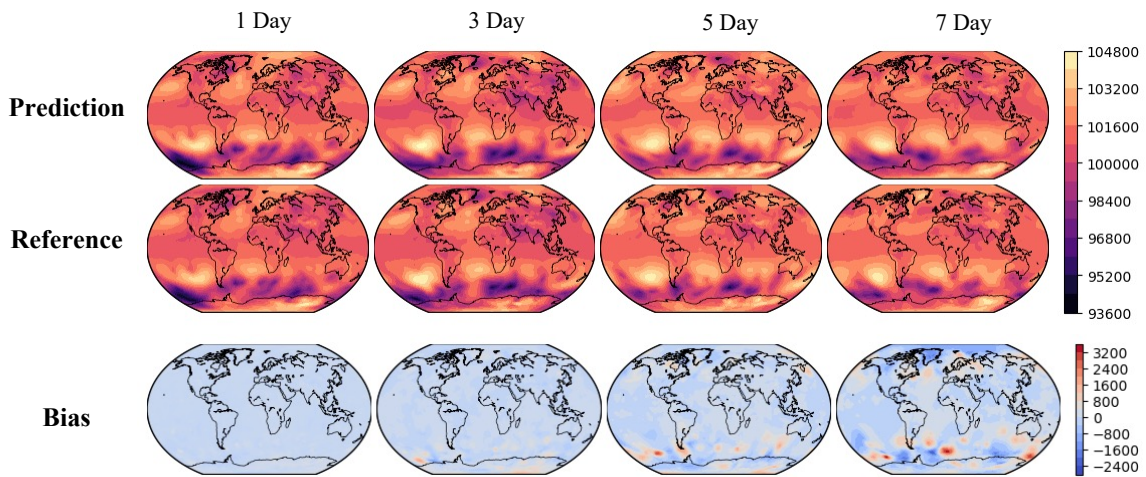
(c) v_{850m} example rollout visualization



(d) t_{850} example rollout visualization



(e) q_{700m} example rollout visualization



(f) MSLP example rollout visualization

Figure C.6: More example rollout visualization of model's prediction versus reference ERA5 reanalysis data at different lead times. The initialization time is 00:00 UTC on August 11, 2020.